

# Dual-purpose architected materials: Optimizing graded BCC lattices for crashworthiness and heat dissipation

Jaswanth V. Gurudev<sup>1</sup> and Ratna Kumar Annabattula<sup>2\*</sup>

<sup>1</sup>Department of Metallurgical and Materials Engineering, Indian Institute of Technology Madras, Chennai, 600036, Tamil Nadu, India.

<sup>2\*</sup>Mechanics of Materials Laboratory, Department of Mechanical Engineering, Indian Institute of Technology Madras, Chennai, 600036, Tamil Nadu, India.

\*Corresponding author(s). E-mail(s): [ratna@iitm.ac.in](mailto:ratna@iitm.ac.in);  
Contributing authors: [vgjaswanth@gmail.com](mailto:vgjaswanth@gmail.com);

## Abstract

Body-centered Cubic (BCC) lattice structures demonstrate promising performance for applications that require simultaneous mechanical energy absorption and thermal management. However, current optimization approaches are typically confined to single-domain objectives, such as mechanical parameters like impact energy and peak stress, neglecting the role of multiple physics in real-world performance. To address this, we propose a multi-objective optimization framework for density-graded BCC lattices that effectively dissipates heat while maximizing absorbed impact energy. A parametric three-zone lattice configuration is investigated to explore various trade-offs between mechanical and thermal properties. Each design is evaluated through independent impact and forced-convection simulations using commercial solvers. Specific Energy Absorption (SEA) and peak stresses at the distal end quantify impact absorption performance, while the Nusselt number and pressure drop characterize thermal dissipation performance. Surrogate models constructed from this data enable multi-objective optimization via Goal Programming to identify an optimal design. Two Pareto-optimal lattice designs are identified with reduced pressure drop and peak stress, underlining the superiority of strategic density gradation. Analysis of the optimal designs reveals how material distribution and geometric design variables influence mechanical-thermal trade-offs, establishing quantitative design guidelines for lattice structures in this multi-physics application.

**Keywords:** Functionally-graded (FG) lattice structures, Multi-physics optimization, Surrogate modeling, Goal programming

## 1 Introduction

The physical properties of metamaterials (specifically mechanical metamaterials) are often dictated by their intricate internal geometries and high specific surface areas. The ability to control the geometry enables the design of structures with tailored mechanical, thermal, and even multi-functional attributes that are unattainable with conventional monolithic counterparts [1]. Such materials exhibit properties

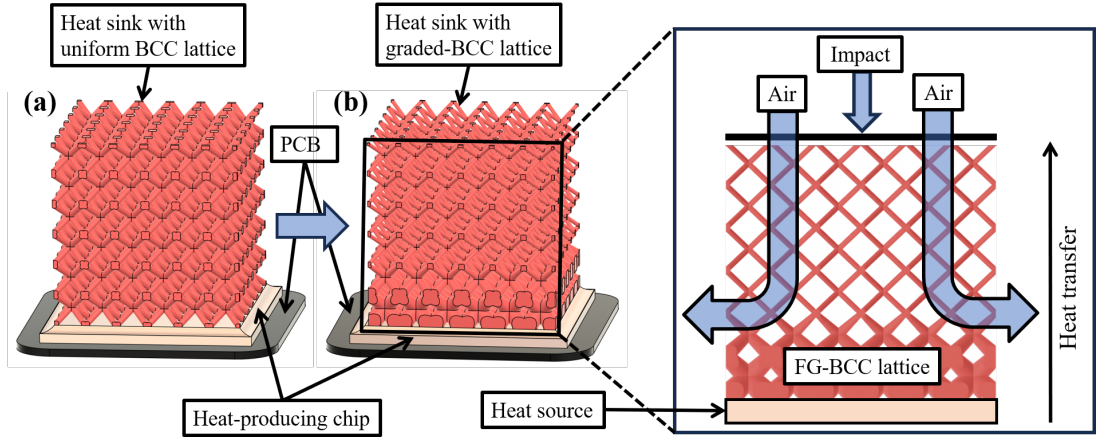


**Fig. 1** A BCC lattice-based heat sink consisting of (a) uniform struts is replaced with (b) a lattice consisting of diameter-graded struts. A cross-section of the hypothesized FG-BCC lattice with a density gradient is also .

that are not typically found in nature and are often the result of purpose-driven designs, having found applications in aerospace [2–5], automotive [6–9], biomedical, and thermal management systems [10–13].

Lattice structures, a class of metamaterials, are gaining prominence for their tunability, especially since the advent of additive manufacturing [14]. While known for crashworthiness, they are increasingly explored for thermal dissipation as traditional heat sinks face limitations from rising power densities [15]. Compared to other cellular structures like metal foams or Triply-Periodic Minimal Surfaces (TPMS), lattices offer a compelling alternative due to their high surface area-to-volume ratio and interconnected pores, which balance efficient thermal conduction with low fluid flow resistance [16, 17]. Studies show lattices can be more efficient heat sinks than conventional finned designs [17–19]. There exist several attempts in the literature to optimize specific topologies, such as BCC lattices, which show superior heat transfer [20], and functionally graded structures, which vary geometry to further enhance thermal performance [14, 15, 21, 22].

Beyond thermal management, lattice structures possess remarkable mechanical properties for energy absorption and crashworthiness. Their performance is characterized by their deformation mechanism: bending-dominated or stretching-dominated [23]. Stretching-dominated structures (such as Octet lattices) exhibit high nodal connectivity, making them weight-efficient and offering superior stiffness and strength for load-bearing applications. Conversely, bending-dominated structures (like BCC lattices) have lower connectivity, offering less resistance to bending, which is ideal for energy absorption [24, 25]. The capacity of lattices to endure large compressive strains at a near-constant stress makes them suitable for protective applications [26, 27]. Researchers are maximizing specific energy absorption by exploring configurations such as BCC and Octet lattices, applying functional grading, developing novel hybrid structures (e.g., FCC-BCC), and using topology optimization to achieve uniform performance regardless of impact direction [26–32].

Due to the numerous possibilities in lattice cell topologies, dimensions, and spatial arrangements, it is often not feasible to conduct experiments or even numerical simulations, given the associated costs and time. To address this issue, significant efforts have been made to utilize surrogate modeling as a powerful technique to interpolate between discrete simulation/experimental data points, especially for improving the crashworthiness of cellular structures [33–38]. However, the potential to tune lattice structures to meet multiple functional requirements simultaneously is often overlooked and remains underexplored. While a particular lattice may not perform the best across all considered functional needs, an optimal design that performs reasonably well with minimal trade-offs can still be achieved. Combining surrogate modeling with multi-objective optimization has been shown to yield such optimal structures [39, 40].

The aim of this paper is to explore the BCC lattice structures for their simultaneous energy absorption and heat dissipation capabilities. To meet the multi-functional requirements mentioned above, we leverage the inherent advantages of the BCC topology, combined with functional grading, to create a lattice that excels at both thermal dissipation and impact absorption. Such structures can be particularly useful in the front-end automotive electronic enclosures (such as Electronic Storage Units (ESUs)) due to strong air convection. Heat sinks made using these lattices for automotive electronic enclosures would prevent severe component damage upon impact, whilst providing superior passive heat extraction.

When referring to the thermal (mechanical) aspect of the lattice, we denote the end of the lattice in contact with the chip as the heat side (support end) and the other end facing the cold incoming air as the air side (impact end). The key idea behind this study is to create an optimized Functionally-Graded BCC (FG-BCC) lattice with thicker struts on the hot side and thinner struts on the cold side. This is beneficial when compared to a BCC lattice with uniform strut diameter in the following ways:

- Thinner struts at the cold side would result in a lower flow resistance during forced convection and would encourage flow mixing within the porous structure of the lattice.
- Thicker struts at the heat side directly translate to improved heat extraction from the heat source (governed by Fourier’s law of heat conduction).

This hypothesis, as illustrated in Fig. 1, drives this study to identify the optimal design variables (diameter values) that simultaneously maximize both thermal dissipation and impact performance, and to examine the trade-offs that arise when designing the lattice for a single application. We define the parameterization of an FG-BCC lattice, describe the simulation frameworks used in this study, formulate an optimization problem, and finally build a surrogate model to identify the Pareto-optimal design for given weights on impact performance and heat transfer.

We start with a BCC lattice made of unit cells of size 4 mm arranged in a periodic  $6 \times 6 \times 6$  grid consisting of struts with a uniform diameter of 0.78 mm (relative density,  $\rho = 0.17$ ). This ‘ground’ lattice configuration is used to reduce computational cost while serving as a reasonable Representative Volume Element (RVE), as concluded by [41] and [42]. The ground lattice will serve as the base structure for evaluating the relative performance of the designed FG-BCC lattices. Numerical simulations of the ground structure were conducted to establish baseline metrics for heat dissipation and energy absorption. Abaqus/Explicit [43] finite element solver was used for the impact simulations. Thermal dissipation performance was evaluated by performing Computational Fluid Dynamics (CFD) simulations using the Ansys Fluent 2025 R1 software [44]. Due to the inherent nature of the problem, trade-offs exist between thermal performance and impact performance, which are discussed in detail. We propose a gradation strategy, as explained in Section 2.1, to explore various relative density gradients across the lattice’s height and determine the optimal lattice design. Multi-objective optimization, aided by surrogate modeling, is employed to simultaneously maximize thermal performance and impact performance by exploring the design space.

## 2 Methodology

To systematically navigate the vast design space and identify optimal lattice configurations, this section formalizes the design variables, describes the simulation setups for both thermal and mechanical analyses, and presents the multi-objective optimization procedure.

### 2.1 Lattice design description

The mechanical and thermal behaviour of lattice structures depends heavily on the nature and degree of gradation of their geometrical features. Here, we vary the relative density of the lattice structure by varying the strut diameter from bottom to top. The FG-BCC lattice structure, consisting of 6 layers (each layer consisting of a  $6 \times 6$  arrangement of FG-BCC unit cells), is divided into three planar zones to effectively explore the design space as shown in Fig. 2. As a result, the rate at which the diameter

changes is not constant throughout the lattice but instead different for all three zones, resulting in four unique diameter values -  $d_0$ ,  $d_1$ ,  $d_2$ , and  $d_3$ , with which the whole lattice structure can be constructed for a given cell size, 4 mm here. Such a setup would allow us to indirectly explore a wide variety of diameter gradients.

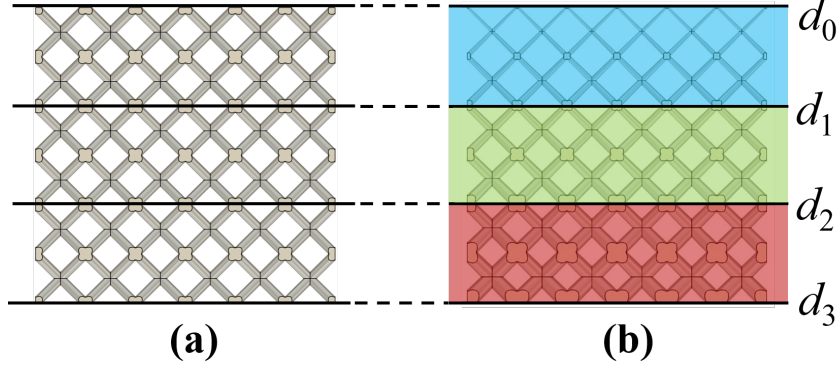


**Fig. 2** The uniform ground lattice (a) is geometrically compared to a discretized FG-BCC lattice (b), consisting of three planar zones. This discretization yields four distinct diameter values:  $d_0$ ,  $d_1$ ,  $d_2$ , and  $d_3$ . These four diameters dictate the geometry of any FG-BCC lattice in this work and will serve as the design variables

To reduce the number of design variables in the problem, we assume  $d_0 = 0.5$  mm, owing to the resolution limit of Additive Manufacturing (AM) techniques [45, 46]. Furthermore, by maintaining the relative density of the FG-BCC lattice the same as the base structure ( $= 0.17$ ),  $d_3$  can be written as a function of  $d_1$  and  $d_2$ , thereby reducing the number of design variables to two. Such a two-dimensional (2D) design space will also enable visualization of the polynomial response surface. An analytical expression for calculating the relative density of FG-BCC lattices is crucial for performing the final step of dimensionality reduction. The relative density of FG-BCC unit cells is generally calculated using the volume fraction of the unit cell. Unfortunately, deriving analytical expressions for calculating the volume occupied by the graded struts is cumbersome due to complex overlap regions at joints and edges. To overcome this problem, we constrain the area fraction rather than the volume fraction in the unit cell. This is done by sectioning the FG-BCC unit cell along the plane with the maximum area fraction, and the analytical expression for the area porosity is calculated as schematically shown in Fig. 3. An FG-BCC unit cell is first cut along its diagonal plane to reveal the smoothly varying strut diameter. We define the large and small diameters at the bottom and top ends of the unit cells as  $D_{\text{large}}$  and  $D_{\text{small}}$ , respectively. Our aim is to project this cross-section onto a 2D plane and calculate the area porosity. To skip the calculation of complex area overlaps and simplify the calculation of the cross-sectional area of the unit cell, we construct an ‘equivalent’ cell with a uniform diameter,  $D$ , that occupies the same cross-sectional area as that of the FG-BCC cell.  $D_{\text{large}}$  and  $D_{\text{small}}$  represent the diameter at the thicker and thinner ends of a strut that intersect the opposite corners of the rectangle as shown in Fig. 3. But, we need the diameters parallel to  $D_{\text{large}}$  and  $D_{\text{small}}$  (call them  $D'_{\text{large}}$  and  $D'_{\text{small}}$ ) that lie in the interior of the rectangle. Using a series of geometrical calculations, as explained in Section A, we get,

$$D'_{\text{large}} = \frac{\sqrt{3} \times D_{\text{large}}}{\sqrt{3} - \frac{2\sqrt{2}}{3\sqrt{3}a}(D_{\text{small}} - D_{\text{large}})} \quad (1a)$$

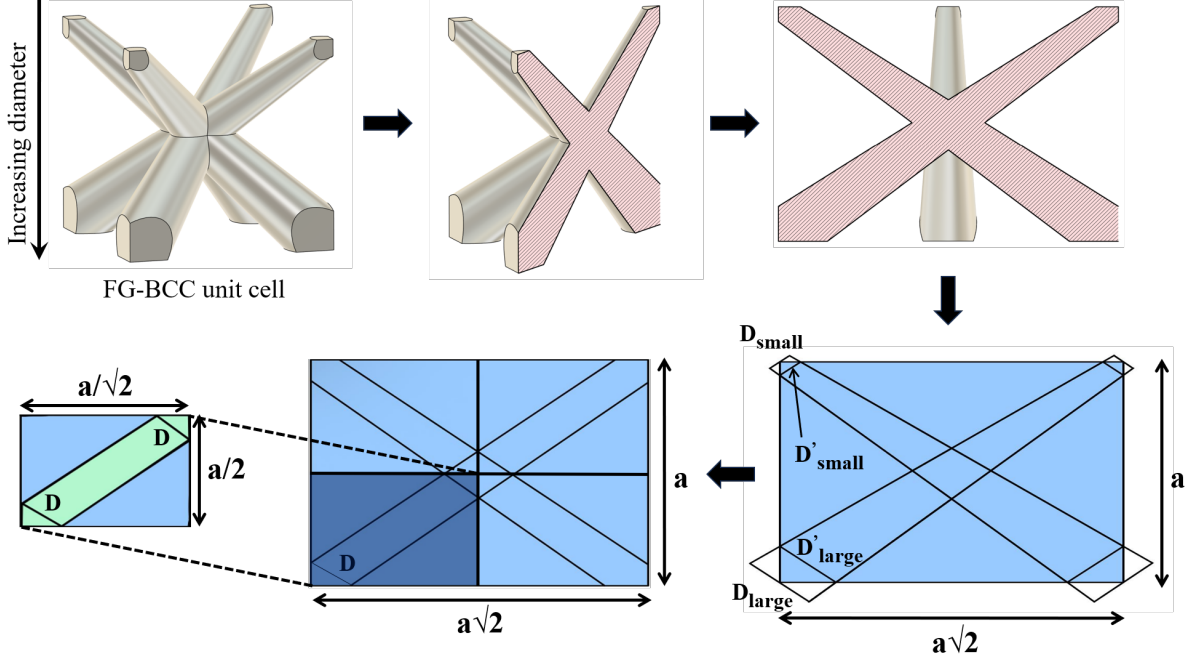


**Fig. 3** Schematic showing the geometric features of an FG-BCC unit cell. The steps shown in the figure outline the simplified process for estimating area porosity, an indirect, approximate measure of relative density

$$D'_{\text{small}} = \frac{\sqrt{3} \times D_{\text{large}}}{\sqrt{3} + \frac{2\sqrt{2}}{3\sqrt{3}a}(D_{\text{small}} - D_{\text{large}})} \quad (1b)$$

where,  $D'_{\text{large}}$  and  $D'_{\text{small}}$  are the inner edge lengths parallel to  $D_{\text{large}}$  and  $D_{\text{small}}$ , respectively. With the inner lengths in hand, the equivalent strut diameter,  $D$ , for the equivalent uniform unit cell is found by taking the average of  $D'_{\text{large}}$  and  $D'_{\text{small}}$  and is given by

$$D = \frac{D'_{\text{small}} + D'_{\text{large}}}{2} = \frac{D_{\text{small}}}{2 + \frac{2\sqrt{2}}{3\sqrt{3}a}(D_{\text{small}} - D_{\text{large}})} + \frac{D_{\text{large}}}{2 - \frac{2\sqrt{2}}{3\sqrt{3}a}(D_{\text{small}} - D_{\text{large}})} \quad (2)$$

The area porosity of the equivalent unit cell is now easily calculated, as explained in [Section B](#). The resulting expression for the area porosity of a unit cell (with a uniform strut of diameter  $D$ ) or, equivalently, our FG-BCC unit cell (whose diameter varies from  $D_{\text{large}}$  to  $D_{\text{small}}$ ) is found to be

$$\text{Area Porosity} = \left(1 - \frac{2D}{a\sqrt{3}}\right)^2 \quad (3)$$

This expression for area porosity will now be used to constrain the relative density for generating new FG-BCC lattice designs. We demonstrate that using this approximate method, new FG-BCC lattices were successfully generated with an error of less than 6% from the target porosity, as shown in [Table 1](#).

## 2.2 Sampling data points using Latin Hypercube Sampling (LHS)

Our objective is to identify the set of  $d_1$  and  $d_2$  that yields the best overall thermal and impact performance. Due to the high computational cost of running a large number of simulations to cover the entire design space, we employ surrogate modeling to approximate optimal diameter values. Out of the multitude of options, we chose the polynomial response surface method, Thin Plate Spline - Radial Basis Functions (TPS -RBF), due to its overall simplicity and effective interpolation. To achieve a reasonably accurate fit for the surrogates, we select 16 random sample points: 4 to represent the corners of the design space and the remaining 12 uniformly within its bounds. The lower bound of  $d_1$ ,  $d_2$ , and  $d_3$  is set to  $d_{\min} = 0.5$  mm, the same as that of  $d_0$  due to manufacturing constraints. The upper bound is identified by setting three out of the four diameter values to 0.5 mm and computing the fourth diameter value subject to the relative density constraint to represent the maximum allowable diameter. Upon calculation using Equation (2) and Equation (3), we get  $d_{\max} = 2.58$  mm as our upper bound for all  $d_1$ ,  $d_2$  and  $d_3$ . We also set  $d_0 < d_1 < d_2 < d_3$  to serve our hypothesis of having thicker struts at the base. This naturally results in  $d_1 \in [d_0, d_2]$ ,  $d_2 \in [d_1, d_3]$  and  $d_3 \in [d_2, 2.58]$ . To choose 16 points within our bounds as defined above

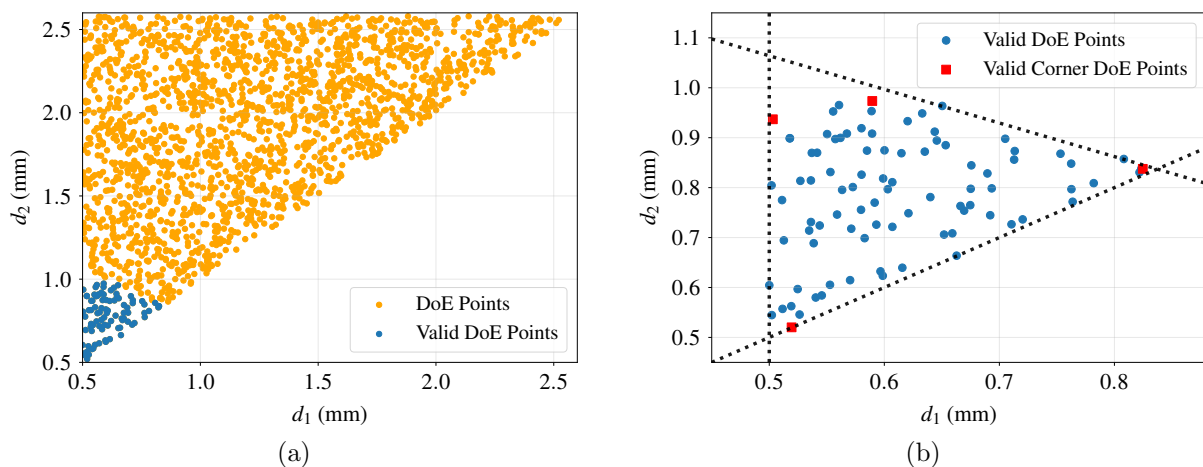


**Fig. 4** (a) The set of all  $(d_1, d_2)$  DoE points (with  $d_1 < d_2$ ) generated using LHS (orange) and the set of valid DoE points satisfying the area porosity constraint (blue), and (b) the zoomed-in plot of all valid points showing the naturally arising feasible region bounded by the dotted lines and red corner points

and subject to density constraints, we first generate a large number of  $(d_1, d_2)$  points within the range  $[0.5, 2.58]$  as shown in Section 2.2. This is achieved using Latin Hypercube Sampling (LHS) to generate uniformly distributed points. Once this is done, we take each and every  $(d_1, d_2)$  point, and then compute  $d_3$  for  $\rho = 0.17$  (the corresponding area porosity = 0.399) along with  $d_0 = 0.5$  mm. If there exists a suitable  $d_3$  in the range  $[d_2, 2.58]$ , then the corresponding  $(d_1, d_2)$  point is further considered for the next round of filtering. Once the set of all  $(d_1, d_2)$  points that satisfy the constraints is generated, we now select four points representing the four corners of our newly obtained feasible region, which is now an embodiment of all the constraints we have defined. Section 2.2 displays the points that meet the relative density constraint, with the feasible region outlined and the four corner points marked in red. The remaining 12 points are chosen using the Greedy Poisson Disk (GPD) method (which utilizes the concept of minimum distance to choose uniformly spaced points in our feasible region, given by the corner points) and highlighted in green along with the four red corner points as shown in Fig. 5. The final list of the 16 selected points showing the  $d_0$ ,  $d_1$ ,  $d_2$ , and  $d_3$  values along with the deviation in the porosity from the ground structure (resulting from our approximation) is shown in Table 1. Now that we have obtained a

**Table 1** The final design points,  $(d_1, d_2)$ , considered for the training dataset, including the ground structure

Lattice ID	$d_0$ (mm)	$d_1$ (mm)	$d_2$ (mm)	$d_3$ (mm)	Porosity (%)	Mass (g)	Porosity Error (%)
0	0.780	0.780	0.780	0.780	82.950	6.250	–
1	0.500	0.503	0.937	1.381	81.141	7.068	2.182
2	0.500	0.825	0.838	0.871	82.670	6.510	0.338
3	0.500	0.519	0.520	2.452	78.010	8.260	5.955
4	0.500	0.589	0.975	1.456	81.950	6.830	1.194
5	0.500	0.669	0.754	1.393	81.790	6.840	1.398
6	0.500	0.513	0.694	1.956	79.730	7.620	3.218
7	0.500	0.705	0.898	0.996	82.430	6.600	0.629
8	0.500	0.537	0.814	1.582	80.910	7.180	2.459
9	0.500	0.616	0.640	1.817	80.490	7.330	2.966
10	0.500	0.615	0.869	1.261	81.880	6.810	1.289
11	0.500	0.764	0.772	1.137	82.410	6.610	0.651
12	0.500	0.593	0.726	1.652	80.910	7.170	2.459
13	0.500	0.524	0.597	2.199	78.940	7.920	4.834
14	0.500	0.690	0.828	1.177	82.220	6.680	0.880
15	0.500	0.603	0.797	1.454	81.470	6.970	1.784
16	0.500	0.557	0.897	1.334	81.520	6.940	1.723

set of 16 sampled points, we design CAD models for all 16 points  $(d_1, d_2)$  and then perform both impact and forced convection simulations, which will be used as training data to fit the surrogate model.

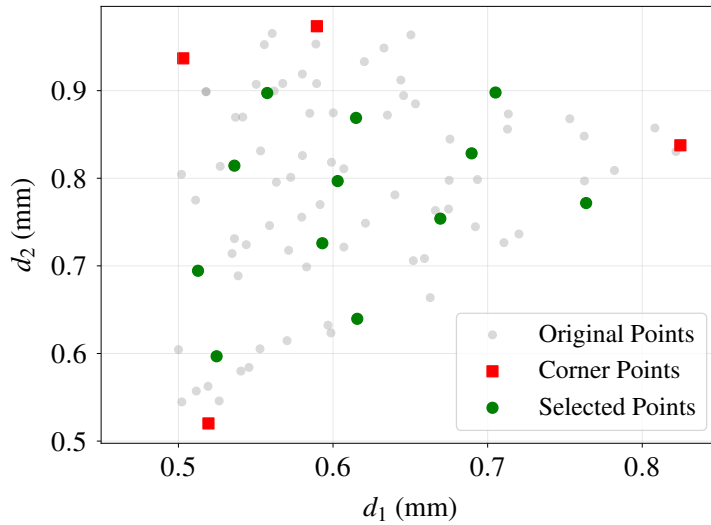


**Fig. 5** The final set of 16 evenly spaced  $(d_1, d_2)$  points (shown in green) in our feasible region represents our training geometries

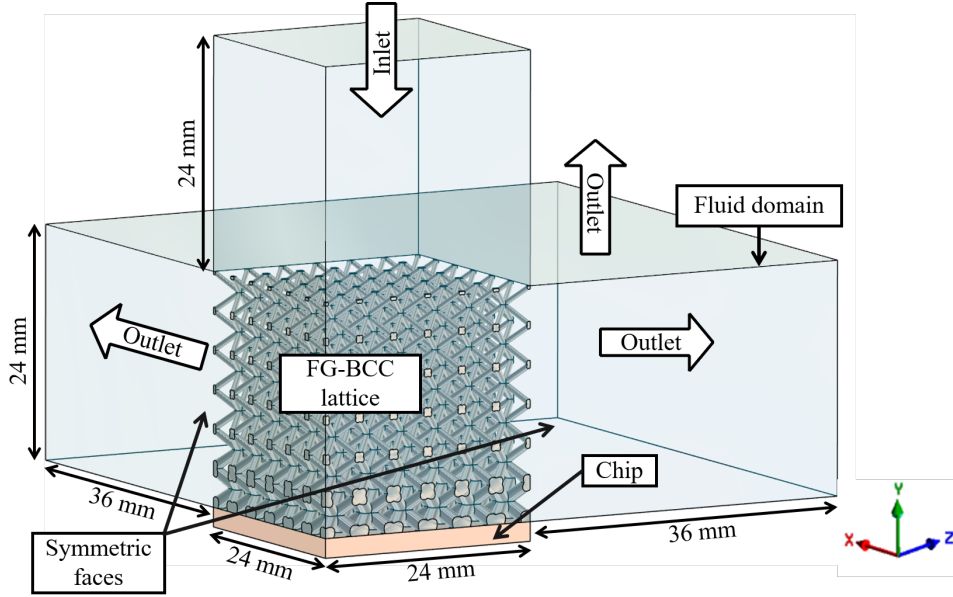


**Fig. 6** The forced convection simulation setup in Ansys Fluent comprising the FG-BCC-16 lattice

### 2.3 Forced convection simulation

Ansys Fluent 2025, a commercial software, was used to perform three-dimensional numerical simulations of forced convection in a jet impingement setup. A thin copper chip serves as the heat source, and the lattice to be tested is placed on top of it. The interface between the chip and the lattice is thermally coupled to prevent heat loss from the chip to the lattice (i.e., zero thermal resistance). Fluid (here, air) is forced through a square inlet directly from the top of the lattice along the -ve y direction, and the outlet is modeled to be all around the lattice. The outlet faces are maintained at 0 Pa. Only a quarter of the whole domain is considered owing to the symmetrical nature of the flow. The adjacent faces in contact with both the chip and lattice are set to be symmetric surfaces. The chip is assumed to be made of copper, and the lattice is considered to be made of Al-6061-T6 alloy. The detailed material properties for both the forced convection and impact simulations are listed in [Table 2](#).

The inlet is positioned 24 mm above the lattice, and the outlets are 36 mm apart in the x and z directions to allow sufficient flow development and prevent reverse flow. Air at 303 K (30 °C) is forced from the top at a velocity of 15 m/s. The geometric setup for the forced convection simulation is shown in [Fig. 6](#). The chip is considered to be an infinite plate of negligible thickness that generates a uniform, constant heat flux of roughly 86,806 W/m<sup>2</sup>. Additionally, due to relatively low fluid velocity 15 m/s (or Mach 0.045) and as the local velocities in the lattice are well below the Mach threshold of 0.3 or roughly 100 m/s as shown in [Fig. 14](#), for all practical purposes, air is assumed to be incompressible [47], and as a result, no density variations exist ( $\rho$  is a constant). It is also assumed that the thermophysical properties of air are independent of temperature. Radiative heat transfer and buoyancy effects, which would result in natural convection due to density fluctuations, are also neglected. Simulations are performed under steady-state conditions. The SIMPLEC scheme was used to solve the pressure-velocity-coupled equations, and the second-order upwind scheme was employed in high-gradient boundary regions. The simulations were run till 1000 iterations or till the value of the continuity equation reached  $10^{-4}$ . The convergence of the chip's bulk temperature and the pressure drop across the lattice was also used to decide the termination of the simulation.

**Table 2** Material properties of Al-6061, Cu and Air

Material	Specific heat capacity (J/kg·K)	Thermal conductivity (W/m·K)	Density (kg/m <sup>3</sup> )	Young's Modulus (GPa)	Yield Strength (MPa)	Poisson's Ratio
Al-6061	871	202.40	2719	70	221	0.32
Cu	381	387.60	8978	117	70	0.33
Air	1006	0.0242	1.225	–	–	–

### 2.3.1 Governing equations

The SST (Shear Stress Transport) k-omega turbulence model is a highly versatile and widely used model in ANSYS Fluent for a broad range of CFD simulations. It effectively combines the best attributes of both the standard k-omega and k-epsilon models. The SST k-omega model excels at predicting flow behaviour in the near-wall region, making it particularly well-suited for applications where boundary-layer effects, flow separation, and adverse pressure gradients are significant, such as in aerodynamics and turbomachinery. By transitioning to a k-epsilon formulation in the free-stream, it avoids some of the limitations of the standard k-omega model, offering a robust and accurate solution for complex industrial flows without being overly computationally expensive. The model combines the k-omega and k-epsilon models using a blending function. The analytical expressions for the continuity equations for mass conservation and transport equations for momentum conservation (along with their blending function) are as follows:

1. Continuity equation:

$$\nabla \cdot \rho \mathbf{u} = 0 \quad (4)$$

2. Transport equations:

The kinetic energy ( $k$ ) - transport equation is:

$$\frac{\partial(\rho k)}{\partial t} + \frac{\partial(\rho u_j k)}{\partial x_j} = P_k - \beta \rho \omega k + \frac{\partial}{\partial x_j} \left[ \left( \mu + \frac{\mu_t}{\sigma_k} \right) \frac{\partial k}{\partial x_j} \right] \quad (5)$$

where  $k = 1 \text{ m}^2/\text{s}^2$  is the turbulent kinetic energy,  $\rho$  is the density of the fluid,  $u_j$  is the mean fluid velocity,  $\omega = 1 \text{ s}^{-1}$  is the specific dissipation rate,  $\beta = 0.09$  is a model constant,  $\mu$  and  $\mu_t$  are bulk and turbulent viscosity ( $\mu_t/\mu = 10$ ), respectively,  $\sigma_k = 0.9$  is the turbulent Prandtl number for  $k$  and  $P_k$  is the turbulent kinetic energy production term.

The specific dissipation rate ( $\omega$ ) - transport equation is:

$$\frac{\partial(\rho \omega)}{\partial t} + \frac{\partial(\rho u_j \omega)}{\partial x_j} = \frac{\partial}{\partial x_j} \left[ \left( \mu + \frac{\mu_t}{\sigma_\omega} \right) \frac{\partial \omega}{\partial x_j} \right] + \frac{\gamma}{\nu_t} P_k - \beta \rho \omega^2 + 2(1 - F) \frac{\rho \sigma_\omega^2}{\omega} \frac{\partial k}{\partial x_j} \frac{\partial \omega}{\partial x_j} \quad (6)$$

where  $\sigma_\omega = 1.0$  is the turbulent Prandtl number for  $\omega$ ,  $\gamma$  is the production coefficient, and  $\nu_t = \mu_t/\rho$  is the turbulent dynamic viscosity. We use a blending function,  $(1 - F)$ , to switch from the k-epsilon model when away from a wall (free stream region) to the k-omega model when close to a wall. When  $F = 1$ , the final term of Equation (6), called the cross diffusion term, becomes zero, and hence serves as the transport equation for  $\omega$ , like the k-omega model. When moving away from the wall, i.e.,  $0 \leq F < 1$ , the cross diffusion term remains, and mimics the behaviour of the  $\epsilon$ -equation by introducing a coupling between  $k$  and  $\omega$ , similar to the way  $\epsilon$  behaves in the k-epsilon model. Due to the steady-state assumption, the time derivative term in the transport equations becomes zero.

### 2.3.2 Metrics of interest for thermal problem

Forced convection setups, especially in our case, involve an air pump at the top of the lattice to push air through its pores. The power required to push air through the lattice is directly proportional to the

cube of the pressure drop across the lattice, i.e.,  $\text{Power} \propto (\Delta P)^3$ , as observed in many experiments involving simpler setups. A lower power requirement is, hence, tied to a lower pressure drop across the lattice, defined as the average pressure difference between the inlet and the outlet. Due to the outlet being connected to the atmosphere ( $P_{\text{out}} = 0 \text{ Pa}$ ),

$$\Delta P = P_{\text{in}} - P_{\text{out}} = P_{\text{in}} \quad (7)$$

where  $P_{\text{in}}$  is the area-weighted averaged pressure at the fluid inlet of the setup and  $P_{\text{out}}$  is the area-weighted averaged pressure at the fluid outlet of the setup. Another measure of flow resistance is the unit-less coefficient of friction,  $C_f$ , given by

$$C_f = \frac{2\Delta P}{\rho U_{\text{in}}^2} \quad (8)$$

where,  $\rho$  is the fluid density and  $U_{\text{in}}$  is the fluid velocity at the inlet. The Nusselt number is given by,

$$\text{Nu} = \frac{hL}{k_f} \quad (9)$$

where  $L$  is the characteristic length,  $k_f$  is the thermal conductivity of the fluid, and  $h$  is the overall heat transfer coefficient along the solid-fluid boundary given by,

$$h = \frac{Q}{A(T_{\text{out}} - T_{\text{in}})} = \frac{q}{T_{\text{out}} - T_{\text{in}}} \quad (10)$$

where  $q$  is the heat flux across the solid-fluid boundary. We can also define an effective thermal performance factor,  $\beta$ , to take into account both the heat transfer and the power requirement aspects as used in [15], given as

$$\beta = \frac{\text{Nu}}{C_f^{1/3}} \quad (11)$$

### 2.3.3 Mesh convergence

The number of elements and the quality of the mesh in the simulation model can significantly impact the accuracy of the results. Patch-independent tetrahedral elements were used to mesh the whole model. Upon meshing, it was found that the skewness was at most 0.84 and the lowest orthogonal quality was 0.15. Typically, having more cells helps obtain an accurate result, albeit at the cost of increased computational time. To balance accuracy and computational cost, we conduct mesh convergence studies to determine the optimal number of cells, beyond which additional cells yield negligible improvements in variable values. Here, we have used the volume-averaged chip temperature and inlet pressure as convergence criteria for the forced convection simulation, with an inlet velocity of 1 m/s. Since the lowest dimension in our design is 0.5 mm at the inlet, we use at least 2 cells across the strut's cross-section for accuracy. Adaptive sizing was used to gradually increase the element size from 0.25 mm in regions of higher geometric complexity to 2 mm in areas of lower geometric complexity. Using two cells across the inlet strut's cross-section yielded approximately 4.84 million cells, which met the minimum required number. The number of cells was slowly increased by decreasing the minimum cell size to study convergence. As a result, we see that beyond 5.5 million elements, the variables of interest do not improve drastically as shown in [Table 3](#). Hence, we proceed with using 5.5 million cells for the forced convection simulations.

## 2.4 Impact simulation

Dynamic crushing simulations were carried out using a commercial finite element software, Abaqus/Explicit, to study the energy absorption of the FG-BCC lattices. As illustrated in [Fig. 7](#), the simulation

**Table 3** Mesh convergence results for forced convection simulation in ANSYS Fluent.

Number of cells (millions)	Avg. Chip Temp. (K)	% change	Inlet Pressure (Pa)	% change
4.84	337.766	–	4.4284	–
5.50	337.341	0.130	4.4482	0.450
7.00	337.328	0.004	4.4505	0.052

consists of the FG-BCC lattice of interest placed between two rigid plates, one plate fixed at the bottom and the other plate moving towards the fixed plate at a constant velocity of 15 m/s, crushing the FG-BCC lattice placed in between. Most car accidents occur below 40 mi/hr (18 m/s) [48], and 55 km/hr (15.3 m/s) has been concluded as the critical collision velocity by lawyers with respect to injuries [49]. For these reasons and to ensure similar scenarios for both impact absorption and thermal dissipation, we set 15 m/s as the impact velocity in this study. General surface-to-surface contacts are defined in the simulation setup. Tangential surface interactions are assumed to be frictional, with static and dynamic friction coefficients of 0.2 and 0.15, respectively. Normal surface interactions are assumed to be general hard contacts. The impact plate is restricted to move only in the direction of impact, while the fixed plate remains stationary, with no displacement allowed.

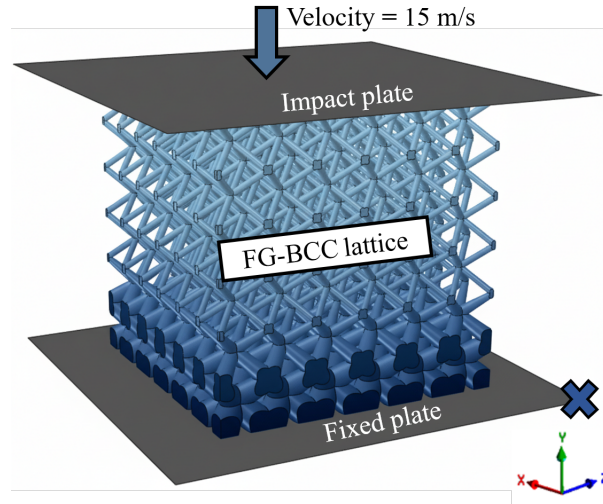


**Fig. 7** Abaqus/Explicit impact simulation setup of an FG-BCC lattice (FG-BCC-3, specifically), colour graded with dark blue at the larger diameter end to light blue at the smaller diameter end, between the fixed and impact plates

The FG-BCC lattice is meshed using linear tetrahedral elements of type C3D4, and the rigid plates using linear quadrilateral elements of type R3D4. Similar to the forced convection simulations, we conduct a mesh-convergence study to determine the optimal mesh size that balances accuracy and computational cost. Impact simulations were performed for the ground FG-BCC lattice meshed with element sizes of 0.5 mm, 0.4 mm, 0.3 mm, 0.25 mm, and 0.225 mm. The total plastic dissipation energy of all these simulations is plotted to visualize the improvement achieved with finer meshes. As evident in Fig. 8, minimal accuracy improvement is observed beyond a mesh size of 0.25 mm; therefore, we use this size for the discretization.

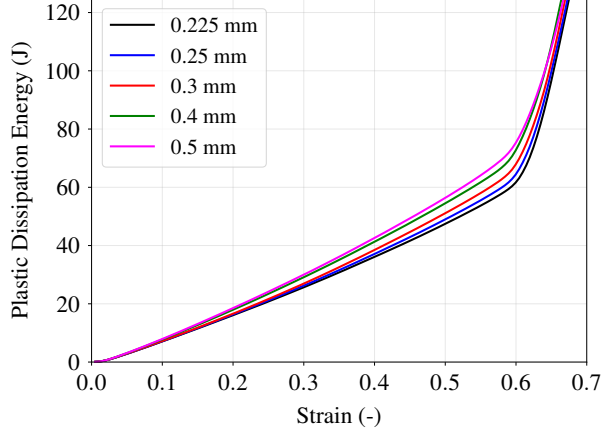


**Fig. 8** Mesh convergence results of impact simulations on the ground BCC lattice showing negligible improvement below an element size of 0.25 mm

### 2.4.1 Material considerations

Al-6061-T6 is a popular choice for mechanical and heat-transfer applications due to its relatively high strength-to-weight ratio, thermal conductivity, and corrosion resistance, especially in heat exchangers. Al-6061-T6 (see [Table 2](#)) is considered to be the strut material for the FG-BCC lattice. A linear-elastic, perfectly plastic material model is assumed for simplicity, and Strain hardening and strain-rate effects are neglected.

### 2.4.2 Metrics of interest for impact problem

Load-versus-displacement data, the most common way to represent the compressive behaviour of cellular structures, is extracted from impact simulations for post-processing. The compressive load experienced by the fixed plate is divided by the initial cross-sectional area of the lattice (24 mm × 24 mm) to calculate compressive stress,  $\sigma$ . Compressive strain,  $\epsilon$ , is calculated by dividing the displacement by the initial lattice length. The stress-strain response of cellular structures under dynamic compression typically consists of three regions: the initial elastic compression; the plastic deformation and collapse of the cellular structure at approximately a steady stress; and, finally, the densification region, where the structure begins to behave similarly to the bulk material. A representative stress-strain curve showing these three regions is shown in [Fig. 9](#). The energy absorbed by the lattice, represented by the Plastic Dissipation Energy (PDE), is extracted from the Abaqus simulation results. Specific Energy Absorption (SEA), defined here as the plastic energy absorbed per unit mass of the lattice ([Equation \(12\)](#)), is a widely used metric for comparing lattice structures based on their impact-absorption capabilities.

$$\text{SEA} = \frac{\text{PDE}}{\text{Mass of the lattice}} \quad (12)$$

The peak stress,  $\sigma_p$ , that the cellular structures experience before the onset of plastic deformation is another important metric of study, see [Fig. 9](#). It represents the maximum stress experienced by the fixed plate (or, in a practical case, the passengers in a vehicle) before or during the initial yielding of a few struts in the lattice. Although the stresses at the fixed end might cross  $\sigma_p$  during the later stages of plastic deformation, the initial  $\sigma_p$  is also associated with the highest amount of jerk (rate of change of acceleration), due to the sharp rise in stress values during the initial stages. High levels of jerk are hazardous, especially for passenger safety. Hence,  $\sigma_p$  is a crucial metric that is examined in depth in this study, and we aim to minimize it.

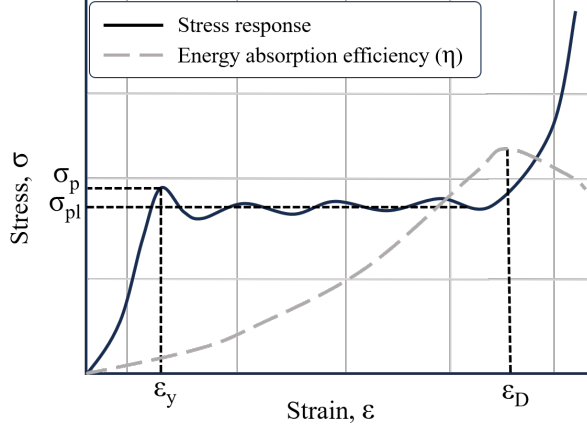


**Fig. 9** A sample stress-strain curve along with its energy absorption efficiency ( $\eta$ ) curve of a general cellular material under compression

The onset strain of densification,  $\varepsilon_D$ , marks the beginning of cell wall interaction (see Fig. 9). At this point, the cell walls begin to contact, suppressing the deformation mechanisms that characterize the plateau region of the stress-strain curve and enhancing the material's compressive resistance. We do not use the term 'densification strain,' as it refers to a more advanced stage in which the cellular material is fully compacted. At this strain, the cell walls are jammed together, leading to a steep increase in the slope of the stress-strain curve. Beyond the densification strain, the compressive properties of the cellular solid are dominated by the properties of the solid material from which the cell walls are made. Hence, the onset strain of densification is another crucial parameter for evaluating the impact absorption performance of cellular structures [50]. Various methods to find  $\varepsilon_D$  are defined in the existing literature. Out of these, we use the definition given by Tan et al. [51], which defines  $\varepsilon_D$  as the stationary point at which the Energy Absorption Efficiency ( $\eta$ ) reaches a global maximum. The energy absorption efficiency ( $\eta$ ) is defined as the energy absorbed up to a given nominal strain,  $\varepsilon_a$ , normalized by the corresponding stress value as follows:

$$\eta(\varepsilon_a) = \frac{1}{\sigma(\varepsilon_a)} \int_0^{\varepsilon_a} \sigma(\varepsilon) d\varepsilon \quad (13)$$

$$\left[ \frac{d(\eta(\varepsilon))}{d\varepsilon} \right]_{\varepsilon=\varepsilon_D} = 0 \quad (14)$$

Upon crossing the onset strain of densification, the lattice becomes progressively 'less efficient' at absorbing energy. Hence, a lattice structure that absorbs the most energy should exhibit a prolonged plastic deformation region, i.e., higher  $\varepsilon_D$  and, as a result, higher SEA. We shall refer to the value of specific energy absorbed until  $\varepsilon_D$  as SEA in this study, which will also be maximized.

The plateau stress,  $\sigma_{pl}$ , is defined as the average stress experienced by the fixed plate during the plastic deformation of the lattice, i.e., from the onset of yielding to the onset of densification, given by

$$\sigma_{pl} = \frac{\int_{\varepsilon_y}^{\varepsilon_D} \sigma(\varepsilon) d\varepsilon}{\int_{\varepsilon_y}^{\varepsilon_D} d\varepsilon} \quad (15)$$

where, the yield strain,  $\varepsilon_y$ , is the strain corresponding to the value of  $\sigma_p$ .

## 2.5 Surrogate model

Surrogate modeling has been a popular choice for solving optimization problems where generating the training dataset is cumbersome. These training datasets are usually compiled from experimental or simulation data, neither of which can be obtained on a large scale to build a large dataset. Surrogate modeling techniques, especially polynomial response surface methods, excel in this context due to their simplicity and robustness. The Thin Plate Spline Radial Basis Function (TPS-RBF) method is adopted here to overcome the pitfalls associated with noise in higher-order polynomials between training points. The TPS-RBF is a surface-interpolation technique that approximates a 3D surface in our problem and computes intermediate values using radial basis function interpolation. The TPS-RBF response surface,  $S(x, y)$  is defined as

$$\hat{S}(x, y) = \sum_{i=1}^N w_i \phi(\|(x, y) - (x_i, y_i)\|) + a_0 + a_1x + a_2y \quad (16)$$

where  $N$  is the number of training points (or centers),  $w_i$  are training weights, and  $p(x, y)$  is a linear polynomial given by

$$p(x) = a_0 + a_1x + a_2y \quad (17)$$

$\phi$  is the kernel function, defined as  $\phi(r) = r^2 \ln(r)$ ;  $\phi(0) = 0$ , where  $r = \|(x, y) - (x_i, y_i)\|$  is the euclidean distance between a query point  $(x, y)$  and a training center  $(x_i, y_i)$ . Leave-One-Out Cross-Validation (LOOCV) was used to construct a surface robust to new, unseen data points. The quality of the TPS-RBF fit is estimated by computing the Mean Absolute Error (MAE) and the Root Mean Square Error (RMSE) given by

$$\text{MAE} = \frac{1}{N} \sum_{i=1}^N e_i \quad \text{and} \quad \text{RMSE} = \sqrt{\frac{1}{N} \sum_{i=1}^N e_i^2} \quad (18)$$

The error,  $e_i = |S_i(x_i, y_i) - \hat{S}_{-i}(x_i, y_i)|$ , where,  $S_i(x_i, y_i)$  is the actual target at the point  $(x_i, y_i)$  and  $\hat{S}_{-i}(x_i, y_i)$  is the prediction at  $(x_i, y_i)$  from the TPS-RBF model trained without the  $i$ -th sample during cross-validation.

## 2.6 Multi-objective optimization: goal programming

To find the best performing FG-BCC lattice according to our hypothesis, we need to maximize SEA and Nu and minimize  $\sigma_p$  and  $\Delta P$ . To achieve this target, we first construct surrogates for each of the four metrics individually. We then identify the required maximum or minimum of each of the four surrogates that can be obtained in the design space. Let the maximum values of SEA and Nu be  $\overline{\text{SEA}}$  and  $\overline{\text{Nu}}$ , respectively and the minimum values of  $\sigma_p$  and  $\Delta P$  be  $\overline{\sigma_p}$  and  $\overline{\Delta P}$ , respectively.

The concept of goal programming requires that specific targets, or ‘goals,’ are set for each objective. Here, the ideal goals are the previously found optimum values of our four metrics:  $\overline{\text{SEA}}$ ,  $\overline{\text{Nu}}$ ,  $\overline{\sigma_p}$ , and  $\overline{\Delta P}$ . This step generates a vector of ideal goals,  $G = [\overline{\text{SEA}}, \overline{\text{Nu}}, \overline{\sigma_p}, \overline{\Delta P}]$ , which may not be practically attainable. To find the optimal design  $(d_1^*, d_2^*)$  that is as close as possible to the ideal design, we allow deviations from the ideal-defined goals. For each objective,  $j$ , two types of deviations are possible:

- Positive deviation ( $d_j^+$ ): represents over-achievement of the goal
- Negative deviation ( $d_j^-$ ): represents under-achievement of the goal

Each of these unwanted deviations is penalized for each unit of deviation that is observed. For example, in the case of maximizing Nu, we penalize a design,  $j$ , if  $\text{Nu}_j < \overline{\text{Nu}}$ , giving a positive penalty for  $d_j^-$  and a zero penalty for  $d_j^+$ . In the case of minimizing  $\Delta P$ , we penalize a design,  $j$ , if  $\Delta P_j > \overline{\Delta P}$ , giving a positive penalty for  $d_j^+$ , and a zero penalty for  $d_j^-$ . These penalties are user-defined and can be treated as hyperparameters. The essence of goal programming now reduces to minimizing the penalty-weighted

**Table 4** Simulation results of the ground BCC lattice structure

Lattice ID	SEA (kJ/kg)	$\sigma_p$ (MPa)	$\sigma_{pl}$ (MPa)	Nu	$\Delta P$ (Pa)	$C_f$	$\beta$
0	8.68	6.19	10.16	5587.30	632.04	4.59	3362.92

**Table 5** Simulation results for the 16 design points

Lattice ID	SEA (kJ/kg)	$\sigma_p$ (MPa)	$\sigma_{pl}$ (MPa)	Nu	$\Delta P$ (Pa)	$C_f$	$\beta$
1	13.83	4.34	14.69	5747.20	431.19	3.13	3929.43
2	9.87	7.83	11.17	5653.63	506.89	3.68	3662.57
3	1.31	2.08	2.65	5988.10	415.60	3.02	4144.70
4	10.22	4.35	12.91	5653.92	450.45	3.27	3809.75
5	3.37	3.97	6.39	5673.07	454.64	3.30	3810.88
6	1.29	4.38	3.03	5485.81	420.69	3.05	3781.67
7	8.93	5.81	11.85	5737.16	469.24	3.40	3813.54
8	1.35	3.96	3.31	5462.65	428.86	3.11	3741.63
9	2.48	2.88	4.66	5059.10	439.96	3.19	3435.83
10	5.70	4.48	8.78	5592.04	451.69	3.28	3764.61
11	4.38	6.35	8.26	5632.34	485.98	3.53	3700.37
12	3.02	3.33	5.07	5543.46	439.99	3.19	3764.69
13	1.94	2.85	3.39	5440.39	418.16	3.03	3757.90
14	5.04	6.93	7.74	5711.82	462.53	3.36	3814.97
15	2.17	3.89	4.59	5577.95	446.15	3.24	3770.60
16	17.70	3.99	17.33	5630.88	439.90	3.19	3824.32

sum of all deviations,  $Z$ , defined as:

$$Z = \sum_{j=1}^4 P_j^+ d_j^+ + P_j^- d_j^- \quad (19)$$

where,  $j = 1,2,3,4$  denotes the four objective functions of the problem and  $P_j^+$  and  $P_j^-$  are user-defined penalties for each objective function. Note that  $P_j^+$ ,  $P_j^-$ ,  $d_j^+$  and  $d_j^-$  are all non-negative quantities. We use this method to find the optimal design  $(d_1^*, d_2^*)$  that achieves the best compromise with the lowest  $Z$  value for a given set of penalties.

## 3 Results

### 3.1 Simulation results

Dynamic compression and forced convection simulations were performed for all 16 FG-BCC lattice designs, along with the ground BCC design, to obtain the values of SEA,  $\sigma_p$ , Nu, and  $\Delta P$  for each lattice design. The combination of all the design points,  $x_i = (d_1, d_2)_i$  with its corresponding  $y_i$ , where  $i$  represents the  $i^{\text{th}}$  lattice design, forms the training data,  $(x_i, y_i)$  ( $y_i$  being the metric of interest) for running the surrogate algorithm to construct surrogates representing the individual polynomial surfaces in the design space. [Table 4](#) summarises the simulation results for the ground structure, which will serve as the basis for comparison. The simulation results for the remaining 16 design points are shown in [Table 5](#).

### 3.2 Surrogate modeling results

TPS-RBF surrogates were constructed using the methodology described in [Section 2.5](#) for each metric of interest: Nusselt number (Nu), Specific Absorption Energy (SEA), pressure drop ( $\Delta P$ ), and peak stress

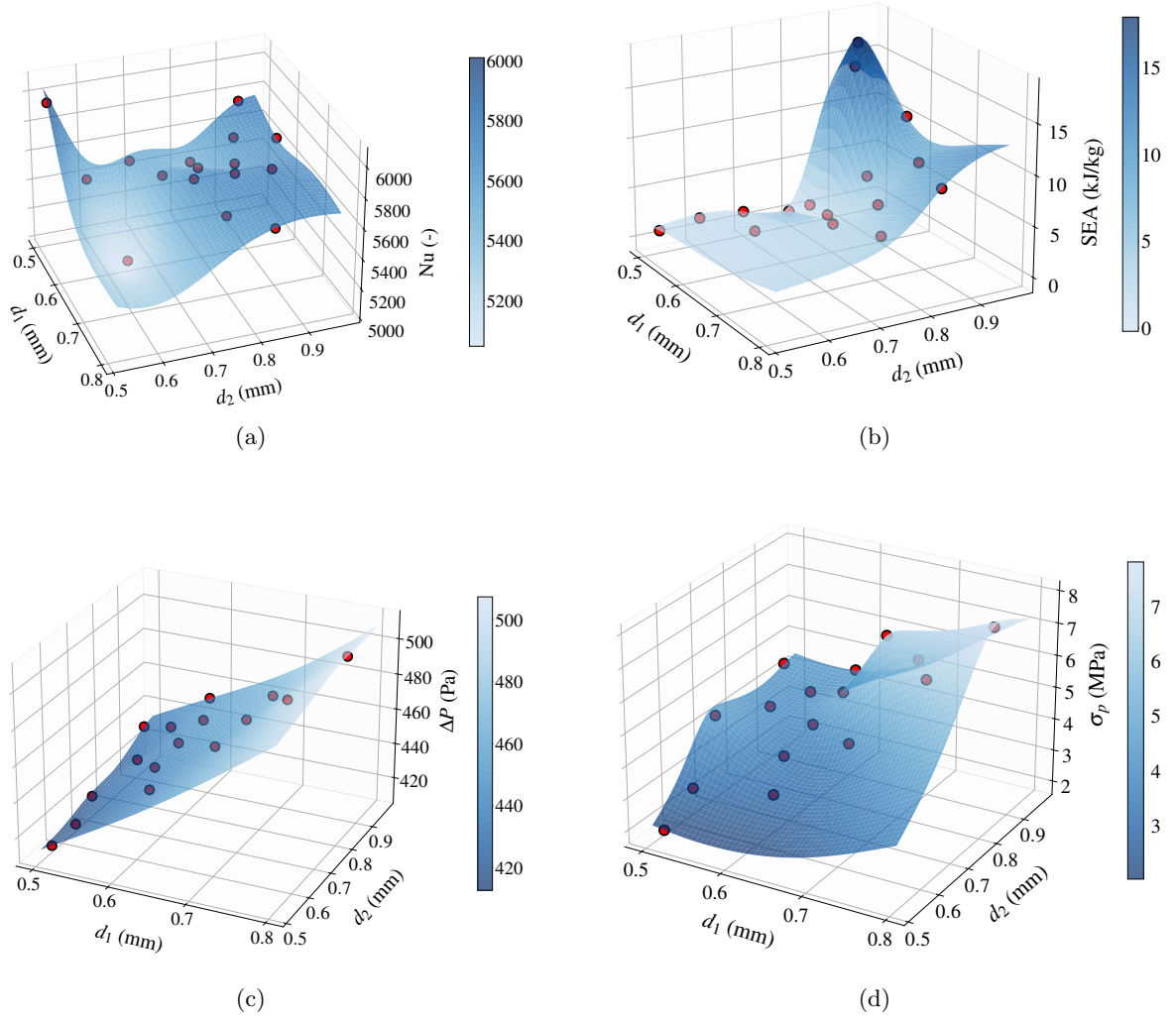


**Fig. 10** Compilation of surface plots of the (a) Nusselt number, (b) maximum specific energy absorption, (c) pressure drop, and (d) peak stress surrogates, constructed using the 16 training points (red) within the design space

( $\sigma_p$ ). The corresponding surfaces are shown in Fig. 10. The  $R^2$  value of all these surrogates is 1.0, and the MAE and RMSE of each of these surrogates are shown in Table 6. These surrogates indicate that the relationship between the metrics and the design variables is highly nonlinear, except for pressure drop, which shows an almost linear trend. The linear nature of the pressure drop function with respect to the diameter values can be explained by the Darcy-Weisbach equation for a flow in a cylindrical pipe, given by

$$\Delta P = f \times (L/d_H) \times \frac{\rho \bar{u}^2}{2} \quad (20)$$

where  $f$  is the friction factor,  $L$  is the characteristic flow length,  $d_H$  is the hydraulic diameter, and  $\bar{u}$  is the mean flow velocity. In our case, for a fixed value of  $d_2$ , as  $d_1$  increases, the resultant pore space through which the fluid flows decreases. As a result, a reduction in the hydraulic diameter,  $d_H$ , is seen.

**Table 6** Surrogate model errors

Surrogate	MAE	RMSE
Nusselt number	3.98e-13	6.82e-13
SEA	2.04e-14	2.90e-14
Pressure Drop ( $\Delta P$ )	5.33e-14	6.19e-14
Peak Stress ( $\sigma_p$ )	2.03e-15	2.85e-15

Hence, as  $d_1$  increases,  $d_H$  decreases, resulting in a linear increase in the pressure drop,  $\Delta P$ . Regarding the Nusselt number surrogate, it can be observed that lattice designs with the smallest  $d_1$  and  $d_2$  values (or the highest  $d_3$  value, due to the relative density constraint) exhibit the highest Nusselt numbers. We also observe that the Nusselt number is more sensitive to  $d_2$  than to  $d_1$ . Specific Energy Absorption (SEA), on the other hand, is higher for designs with a combination of a lower  $d_1$  and a higher  $d_2$ , and the increase in SEA is rapid near the corner values. The peak stress surrogate shows a minimum for designs with the smallest  $d_1$  and  $d_2$  values. These observations precisely match the hypothesis, as described in [Section 1](#). Lattice designs with thinner struts (lower  $d_1$  and  $d_2$  values) at the top exhibit the lowest peak stresses (under impact) and pressure drop (under forced convection), as expected. Additionally, these lattices, with a significantly larger  $d_3$  value (thicker struts at the bottom), exhibit the highest Nusselt number, as expected, due to the increased contact surface area.

### 3.3 Goal programming results

Now that we have the surrogates ready, the maximum values of Nu and SEA surrogates, along with the minimum values of  $\Delta P$  and  $\sigma_p$ , are found using the L-BFGS method. These values will serve as targets, or ‘goals,’ for the multi-objective optimization problem. The identified goals for our problem are given in [Table 7](#). The goal programming algorithm was run with a penalty of 1 (or equal weightage to all metrics)

**Table 7** Goals for multi-objective optimization

$\bar{Nu}$	$\overline{SEA}$ (kJ/kg)	$\overline{\Delta P}$ (Pa)	$\overline{\sigma_p}$ (MPa)
6052.59	18.06	411.83	1.99

for all goal deviations, and the results are shown in [Table 8](#). Here,  $d_1^*$  and  $d_2^*$  are the optimal diameter values. While this optimal design (called O1 hereafter) achieves the best thermal performance and has very low  $\sigma_p$  and  $\Delta P$  values, its SEA value is considerably lower than the target and even the ground structure. This can be attributed to the dominance of the lattice designs, which have the lowest  $d_1$  and  $d_2$  values across three of the four metrics. To achieve a more meaningful tradeoff, we increase the penalty for SEA deviation to 250 and rerun the goal programming algorithm; the results are shown in [Table 9](#). This design (called O2 hereafter) shows a fairly balanced tradeoff in Nu for gain in SEA. Although the value of Nu is significantly lower than the set goal, it is comparable to the ground structure, while all the other metrics have shown substantial improvements. A much more comprehensive comparison of the designs O1 and O2 with the ground structure is given in [Table 10](#). The generated O1 and O2 lattice geometries are shown in [Fig. 11](#). Clearly, the design O2 is better than O1; despite having a minimal improvement ( $\approx 2$  percent) in Nu, it still exhibits an improved overall thermal performance ( $\approx 15$  percent), as indicated by  $\beta$  due to the lower pressure drop.

**Table 8** Goal programming result with equal penalties

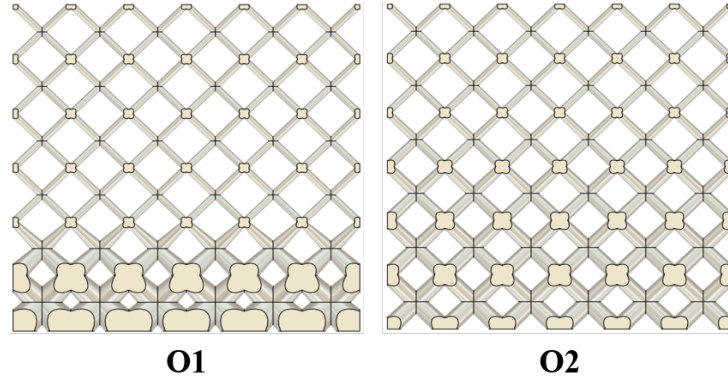
$d_1^*$ (mm)	$d_2^*$ (mm)	Nu	SEA (kJ/kg)	$\Delta P$ (Pa)	$\sigma_p$ (MPa)
0.503	0.520	6052.59	1.16	411.83	1.99

**Table 9** Goal programming result with a higher penalty for SEA deviation

$d_1^*$ (mm)	$d_2^*$ (mm)	Nu	SEA (kJ/kg)	$\Delta P$ (Pa)	$\sigma_p$ (MPa)
0.539	0.919	5679.71	17.22	437.31	4.11

**Table 10** Comparing the performance of optimal lattice designs with the ground lattice

Lattice ID	$d_1^*$ (mm)	$d_2^*$ (mm)	Nu	SEA (kJ/kg)	$\Delta P$ (Pa)	$\sigma_p$ (MPa)	$\beta$
0 (Ground Structure)	0.780	0.780	5587.30	8.68	632.04	6.19	3362.92
O1	0.500	0.520	6052.59	1.16	411.83	1.99	4202.08
% Improvement	-	-	8.33	-88.18	34.84	66.65	24.95
O2	0.539	0.919	5679.71	17.22	437.31	4.11	3865.09
% Improvement	-	-	1.65	114.77	30.81	35.95	14.93

**Fig. 11** The cross-section of O1 and O2 lattice geometries

### 3.4 Simulation results for the O1 and O2 lattice

To evaluate the reliability of our framework, impact and forced-convection simulations were performed on both lattice designs, O1 and O2. The simulation results are presented in [Table 11](#), indicating that the simulation results align well with the goal programming results.

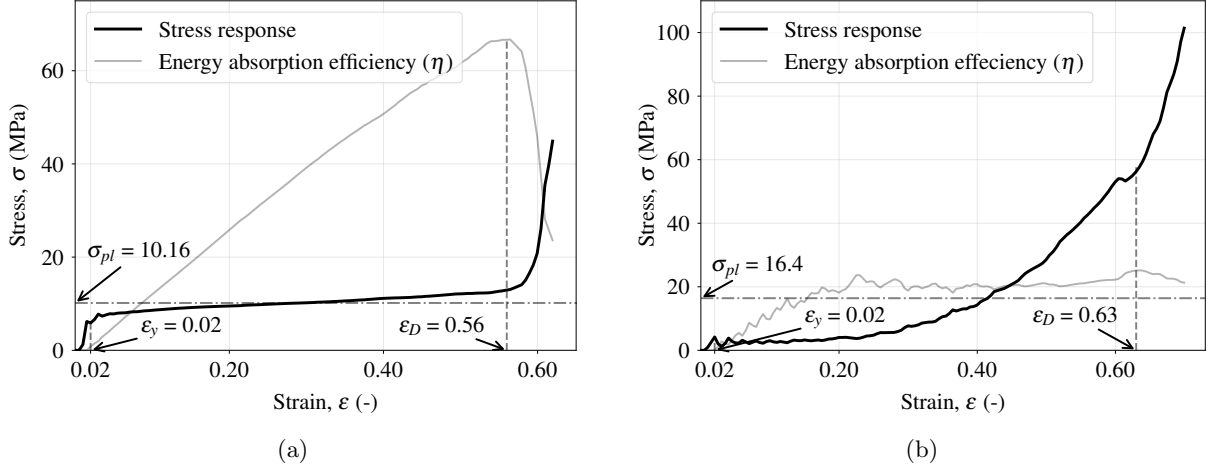
## 4 Discussion

### 4.1 Impact performance

To better understand the reason behind the improvement in the impact performance of the O2 lattice over the ground lattice, the stress-strain plots for both structures are studied, as shown in [Fig. 12a](#) and [Fig. 12b](#), respectively. The sequential deformation of the ground and O2 structures at discrete strain points is shown in [Fig. 13a](#) and [Fig. 13b](#), respectively.

**Table 11** Validation of the goal programming results with simulation results

Lattice ID	$d_1^*$ (mm)	$d_2^*$ (mm)	Nu	SEA (kJ/kg)	$\Delta P$ (Pa)	$\sigma_p$ (MPa)
O1 – GP	0.500	0.520	6052.59	1.16	411.83	1.99
O1 – Simulation	0.500	0.520	6075.59	1.214	417.31	2.352
% Error	-	-	0.38	4.66	1.33	18.19
O2 – GP	0.539	0.919	5679.71	17.22	437.31	4.11
O2 – Simulation	0.539	0.919	5664.37	16.447	443.39	4.203
% Error	-	-	0.27	4.70	1.39	2.26

**Fig. 12** Comparison of stress–strain response and energy absorption efficiency of (a) the ground lattice and (b) the optimized O2 lattice

Key observations from the stress-strain curves are:

- The stress during plastic deformation is almost constant and smooth in the case of the ground structure, but it is continuously increasing with fluctuations in the case of the O2 structure. This can be attributed to the increasing strut diameter along the impact direction in the O2 structure, as opposed to the uniform-diameter struts in the ground structure.
- $\eta$  is almost linearly increasing in the case of ground structure, but it is highly fluctuating, and increases slowly till  $\varepsilon_D$  in the case of the O2 structure.
- The onset strain of densification ( $\varepsilon_D$ ) is higher in the O2 structure than the ground structure, showing that the O2 structure loses its "usefulness" much later than the ground structure, as  $\varepsilon_D$  is defined as the strain at the global maximum of the energy absorption efficiency curve.
- The O2 structure has a lower initial peak stress as compared to the ground structure.

The ground structure exhibits a uniform and steady collapse of all layers together, as shown in Fig. 13a. The O2 structure, on the other hand, as shown in Fig. 13b, has progressive collapse. The collapse of a layer begins only when the collapse of the previous layer has been completed. This layer-by-layer collapse causes the stress values to increase at regular intervals, as fresh struts that have undergone negligible plastic deformation at lower layers are always available, especially in the initial stages of deformation.

## 4.2 Thermal performance

We have so far seen that the O1 lattice has the highest Nusselt number, lowest pressure drop, and also the highest effectiveness,  $\beta$ . Increasing the strut diameter decreases porosity, creating two competing effects.

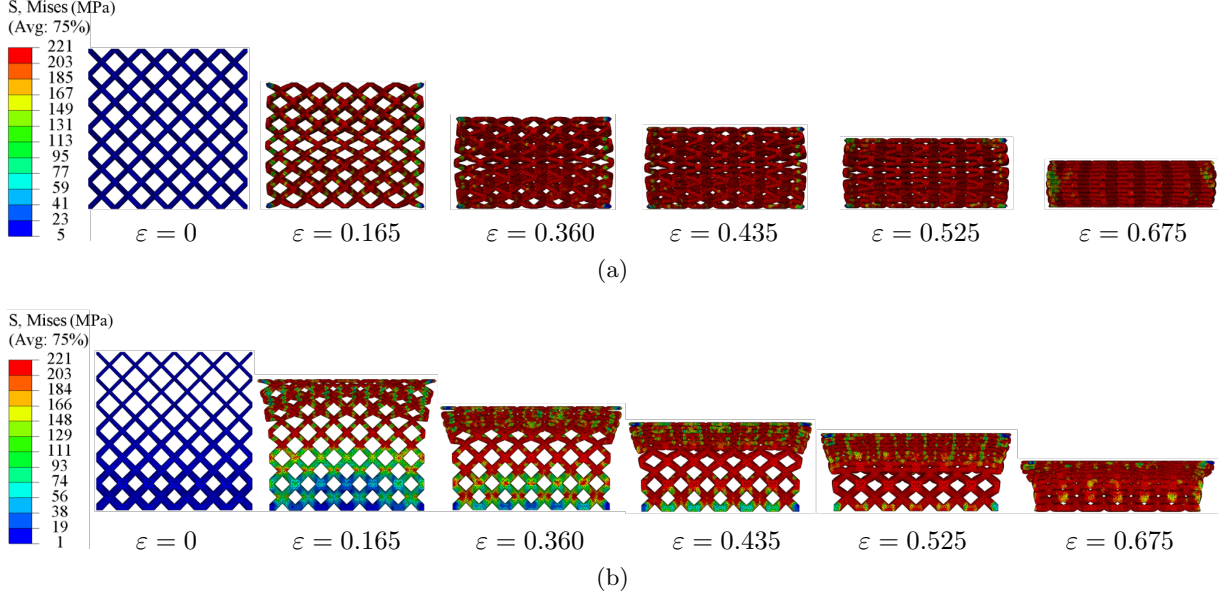


**Fig. 13** Comparative deformation patterns between (a) ground BCC showing uniform stress distribution and consistent compression, and (b) O2 lattice showing stress localization and sequential densification at various strain levels

First, the flow resistance increases, reducing the mass flow rate of the cold air and thus decreasing overall convection. Second, the total surface area in contact with the cold air increases, providing more area for heat transfer and thereby increasing convection. The net thermal performance, therefore, depends on which of these effects is dominant. O1 possesses a significantly larger fluid-contact surface area. While its average fluid velocity is lower (see Fig. 14), this vast increase in area is the primary driver for its high Nusselt number and greater overall convective transfer, far compensating for the velocity-based thermal penalty. O1 also features a larger contact area at the lattice-chip interface. This allows more total heat to be extracted from the chip. However, as shown in Fig. 15, the average steady-state chip temperature is the highest ( $\approx 345$  K) in the case of the O1 lattice, despite its higher Nusselt number. This poor thermal performance can be attributed to flow stagnation. The thicker struts at the bottom of the O1 lattice impede airflow, leading to poor airflow in the critical region directly above the chip. As a result, the incoming air bypasses this restrictive lower zone, mainly flowing through the upper region, as is evident in Fig. 14. The thicker struts also reduce the chip's exposed surface area to the cold air. This localized flow blockage is the dominant effect, starving the chip surface of cold air and preventing effective heat removal, leading to high temperatures. In contrast, the ground ( $\approx 337$  K) and O2 ( $\approx 340$  K) lattices allow for better air circulation to the chip, resulting in lower and more preferable temperatures. The O2 lattice also excels by having a lower pressure drop as compared to the ground structure, as shown in Fig. 16. This is due to the lower flow resistance facilitated by having thinner struts at the top in the O2 lattice. In summary, as compared to the ground lattice, the O1 lattice excels with a higher Nusselt number and a lower pressure drop, but results in a much higher chip temperature, whereas the O2 lattice excels with an almost identical Nusselt number, a lower pressure drop, with only a slight increase in the average chip temperature. The O2 lattice is the clear choice, as it extracts more heat from the chip than the O1 lattice, despite having a lower Nusselt number, resulting in a lower average chip temperature.

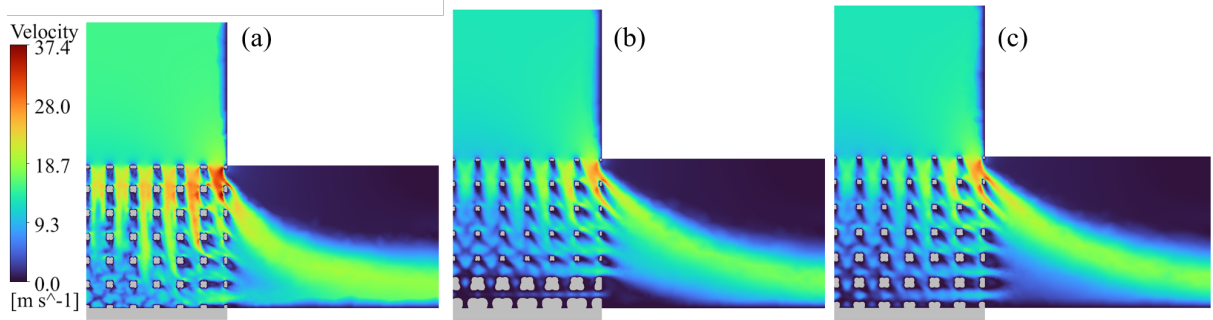


**Fig. 14** Velocity contours are shown on the mid-plane for three types of lattices: (a) the ground lattice, (b) the O1 lattice, and (c) the O2 lattice

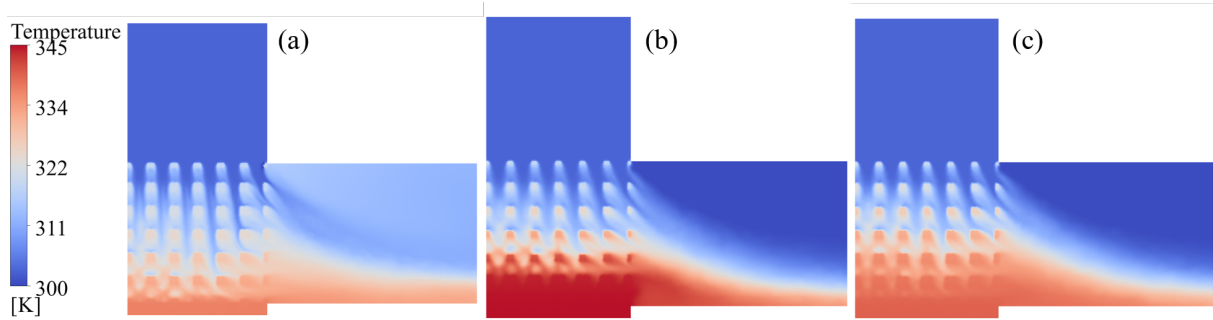


**Fig. 15** The temperature distributions on the mid-plane are illustrated for three scenarios: (a) the ground lattice, (b) the O1 lattice, and (c) the O2 lattice. The chip temperature is notably higher in the case of the O1 lattice

### 4.3 Trade-offs between competing objectives

The O1 and O2 lattices, which are Pareto-optimal designs for different sets of weights, result from carefully balanced trade-offs between impact and thermal performance. A careful examination of the simulation data from the 16 training points is conducted to reveal the geometric features that favor one property over the other. Fig. 17a and Fig. 17b summarize the impact and thermal performance of all 16 training points. As highlighted by the black bounding boxes, the FG-BCC lattices, FG-BCC-16 and FG-BCC-3, exhibit the best performance in impact absorption and thermal dissipation, respectively.

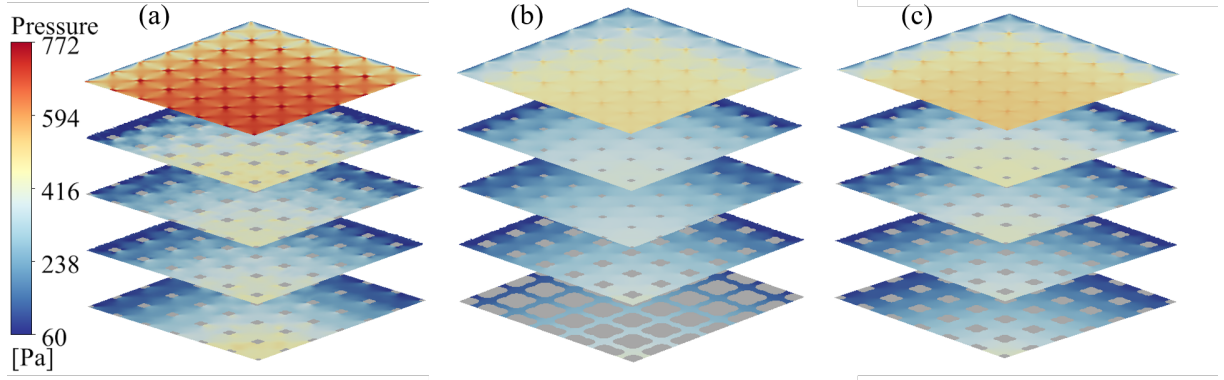


**Fig. 16** The pressure contours at regular height intervals are shown for (a) the ground lattice, (b) the O1 lattice, and (c) the O2 lattice

**Table 12** The design features of lattice-3 and lattice-16

Lattice ID	$d_0$ (mm)	$d_1$ (mm)	$d_2$ (mm)	$d_3$ (mm)
3	0.500	0.519	0.520	2.452
16	0.500	0.557	0.897	1.334

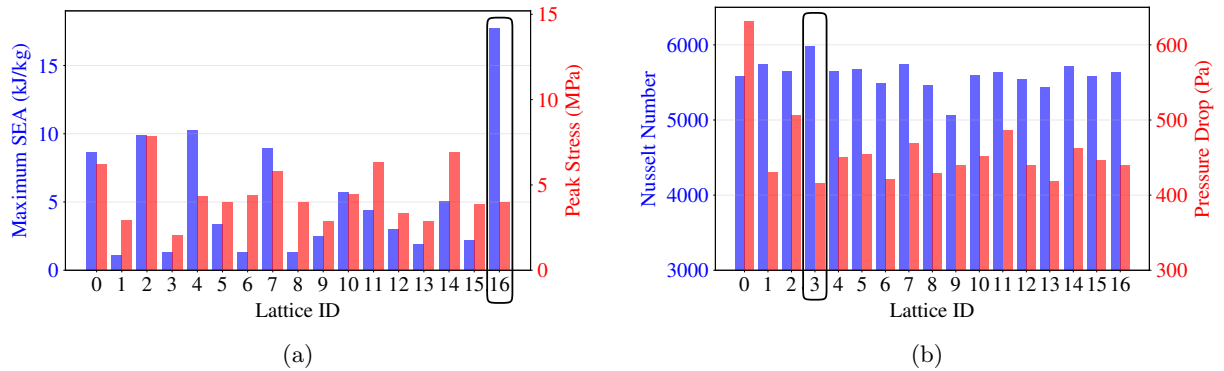


**Fig. 17** Bar plots showing the (a) impact performance (described by maximum SEA and peak stress) and (b) thermal performance (described by Nusselt number and pressure drop) of each lattice design, including the ground lattice

Table 12 shows that these lattices vary significantly in  $d_2$  and  $d_3$ , whereas  $d_1$  is nearly identical, differing by only one decimal place. Moreover, it is to be noted that FG-BCC-3 and FG-BCC-16 have similar diameter values as O1 and O2 lattices, respectively. In the case of FG-BCC-3, the diameter values do not increase significantly until the last diameter ( $d_3$ ), resulting in a steep diameter gradient in the third planar zone closest to the heat source. Due to this, FG-BCC-3's behaviour can be thought to be similar to a compound lattice made by placing a lattice of an almost uniform strut diameter of 0.5 mm placed on top of a second lattice whose struts vary in diameter abruptly to a maximum limit (from  $d_2$  to  $d_3$ ). This last lattice portion behaves almost like a dense solid, with no ability to undergo plastic deformation. This is exactly what is observed in the FG-BCC-3 impact simulation results. Fig. 18a shows

the stress-strain profile for FG-BCC-3 under deformation. We observe an almost flat plateau region due to lattice deformation with very slender struts, until the initial densification at around a strain of 0.4. Then it continues to densify to a strain of 0.6, at which point the collapse of the penultimate unit-cell layer begins, as shown in Fig. 19, resulting in a slight drop in stress, followed by an increase again.

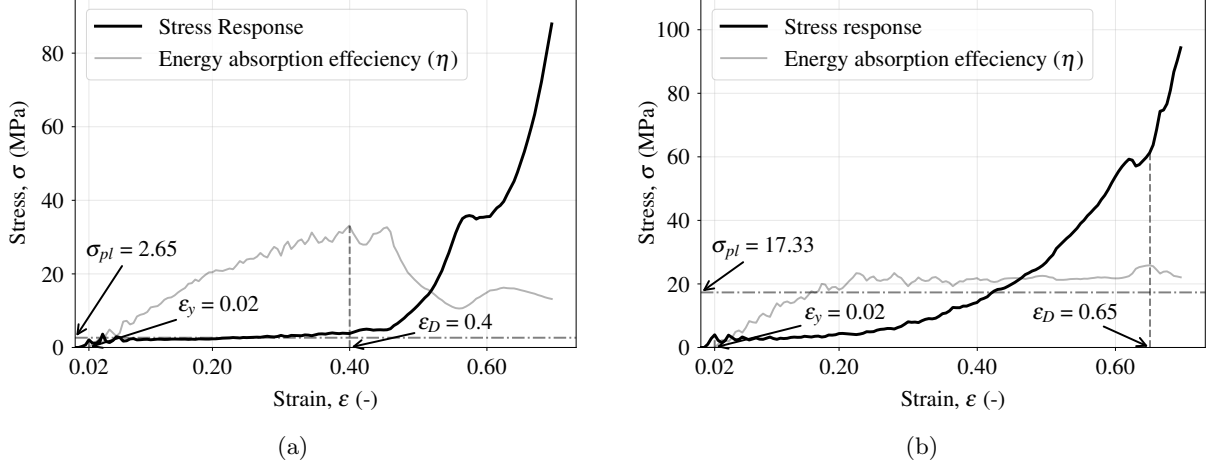


**Fig. 18** The stress-strain and energy efficiency profiles of two lattice types: (a) the FG-BCC-3 lattice demonstrates a significant double densification phenomenon attributed to its compound lattice-like behaviour, while (b) the FG-BCC-16 lattice exhibits deformation similar to the O2 lattice but has a less pronounced second densification phase

This shows that FG-BCC-3 behaves as expected, like a compound lattice. Since the slender section of the lattice undergoes greater strain at very low stress, it absorbs minimal plastic energy, even compared to the ground structure, which has thicker (0.78 mm) but uniform struts than FG-BCC-3. FG-BCC-16, on the other hand, behaves very similarly to the O2 lattice due to the resemblance in diameter values. Hence, as the first couple of layers of FG-BCC-16 are slender, similar to the O2 lattice, the diameter increases steadily, resulting in gradually climbing stress values, as shown in Fig. 18b. Consequently, more plastic energy is absorbed throughout the plastic deformation phase. Hence, although FG-BCC-3 was exceptional in thermal performance, its impact performance is subpar due to its inherent geometry, resulting in a compound-lattice behaviour.

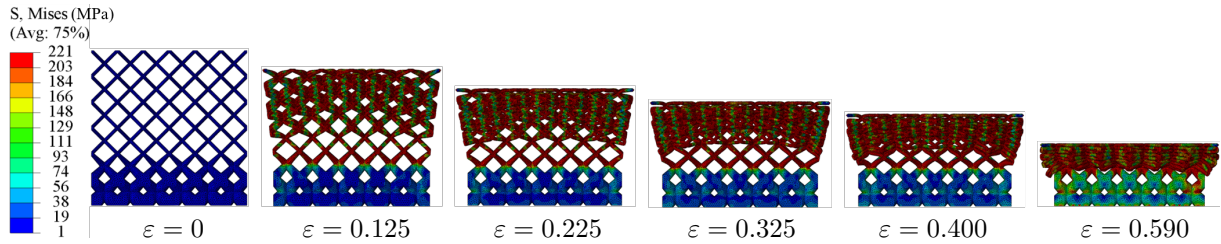


**Fig. 19** The deformation pattern in the FG-BCC-3 lattice, exhibiting a compound lattice-like behaviour

On the other hand, examining the design similarity between FG-BCC-16 and the O2 lattice revealed that it had the best impact performance and an overall improved thermal performance, despite the lower Nusselt number.

## 5 Conclusions and future work

By exploring the possibility of optimizing an FG-BCC lattice using surrogate modeling and multi-objective optimization techniques, we have successfully identified two optimal lattice designs, O1 and O2. In comparison to the ground lattice,

- the O1 lattice is unsuitable for heat extraction, leading to a significant spike in chip temperature (despite an 8% increase in Nu). Furthermore, it performs very poorly under impact, showing an 88% reduction in absorbed energy (SEA). However, it exhibits a lower peak stress ( $\sigma_p$ ) by 67% and pressure drop ( $\Delta P$ ) by 35%;
- the O2 lattice excels in energy absorption, showing a 115% improvement in SEA and a 36% decrease in  $\sigma_p$ . Importantly, it is also effective for heat extraction, maintaining a reasonable chip temperature, and reducing  $\Delta P$  by 31%.

Simulations were performed for the O1 and O2 lattice designs to evaluate the optimization framework, and the results match closely. Evidently, almost all FG-BCC lattice designs exhibit lower pressure drop than the ground lattice, validating the initial hypothesis. We also observe that the FG-BCC with a higher density (steeper density gradients) near the lattice-chip interface (such as the O1 lattice) favors the Nusselt number at the cost of heat extraction (due to poor fluid flow) and impact absorption, whereas the FG-BCC lattice with a linearly increasing density (like the O2 lattice) favors impact absorption and heat extraction. In summary, the O1 lattice’s failure on two of the four primary objectives makes it a poor choice, whereas the O2 lattice excels on all objectives, making it an obvious choice. In this work, surrogate models were used to minimize the need for extensive simulations. Traditional surrogate models often fail to capture complex non-linear patterns without a large dataset, which is computationally expensive. Physics-Informed Neural Networks (PINNs) integrate physical laws but still require numerous sampling points. The use of Physics-Informed Geometric Operators (PIGOs) offers significant promise in this regard. By complementing surrogate models with geometry-informed operators, not only can the dependence on expensive computational simulations be reduced, but new physically consistent training data can also be generated. This enhanced physics-awareness further enables the discovery of higher-order latent variables that govern the lattice properties, beyond simple geometric descriptors such as diameter or cell size. Additionally, this work can be extended to a vast number of novel topologies beyond the traditional ones such as BCC, FCC, and diamond cubic). Significantly, such an approach would extend predictive capabilities to designs outside the originally sampled lattice space, thereby broadening the applicability of computational design frameworks for architected materials.

## A Derivation for the equivalent diameter, $D$

Leveraging the linear variation in diameter over the diagonal of length  $a\sqrt{3}$ , from Fig. 20, we can write,

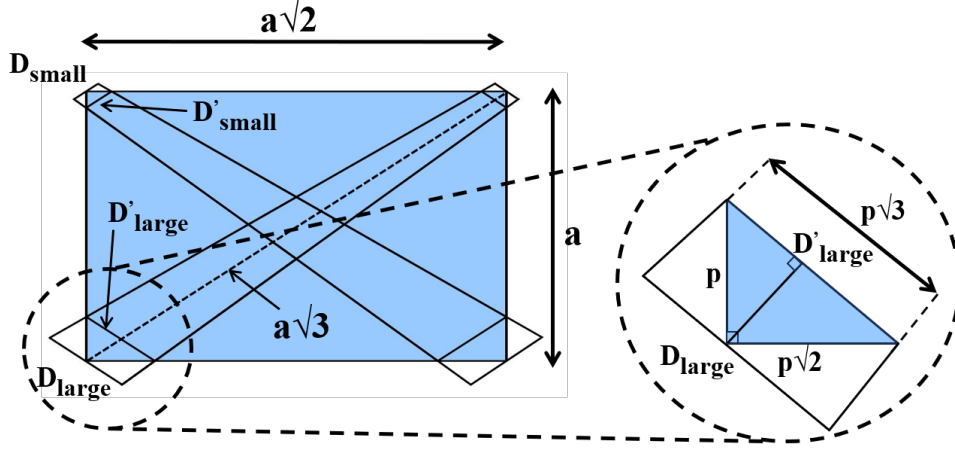


**Fig. 20** The zoomed-in representation is shown to understand the calculation of the parallel interior diameters

$$\begin{aligned}
 D'_{\text{large}} &= p\sqrt{3} = D_{\text{large}} + \frac{p\sqrt{2}}{3a}(D_{\text{small}} - D_{\text{large}}), \\
 p \left[ \sqrt{3} - \frac{\sqrt{2}(D_{\text{small}} - D_{\text{large}})}{3a} \right] &= D_{\text{large}}, \\
 p &= \frac{D_{\text{large}}}{\sqrt{3} - \frac{\sqrt{2}}{3a}(D_{\text{small}} - D_{\text{large}})}, \\
 D'_{\text{large}} &= p\sqrt{3} = \frac{D_{\text{large}}}{1 - \frac{\sqrt{2}}{3\sqrt{3}a}(D_{\text{small}} - D_{\text{large}})}.
 \end{aligned} \tag{21}$$

Similarly, we get,

$$D'_{\text{small}} = \frac{D_{\text{small}}}{1 + \frac{\sqrt{2}}{3\sqrt{3}a}(D_{\text{small}} - D_{\text{large}})}. \tag{22}$$

We find the equivalent diameter,  $D$ , by taking average of  $D'_{\text{small}}$  and  $D'_{\text{large}}$ :

$$D = \frac{D'_{\text{small}} + D'_{\text{large}}}{2} = \frac{D_{\text{small}}}{2 + \frac{2\sqrt{2}}{3\sqrt{3}a}(D_{\text{small}} - D_{\text{large}})} + \frac{D_{\text{large}}}{2 - \frac{2\sqrt{2}}{3\sqrt{3}a}(D_{\text{small}} - D_{\text{large}})} \tag{23}$$

## B Derivation for the area porosity

The area porosity, which is the ratio of the unoccupied area (the blue region) to the total area of the rectangle, is given by

$$\text{Area Porosity} = \frac{2 \times \frac{1}{2}bh}{\frac{a}{\sqrt{2}} \times \frac{a}{2}} \tag{24}$$

where,  $b$  and  $h$  are the dimensions of the blue triangle as shown in Fig. 21, whose lengths are defined as

$$b = \frac{a}{\sqrt{2}} - \frac{\sqrt{2}D}{\sqrt{3}} \quad \text{and} \quad h = \frac{a}{2} - \frac{D}{\sqrt{3}} \tag{25}$$

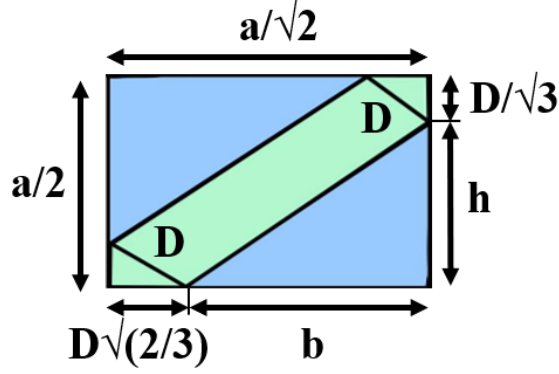


**Fig. 21** One quarter of the cross-section containing an equivalent uniform lattice with struts of diameter,  $D$ , is shown, which occupies the same area as the functionally graded lattice. The area porosity is now simply calculated by dividing the area of the unoccupied blue region by the total area

Simplifying the expression, the area porosity is finally given by

$$\text{Area Porosity} = \frac{2 \times 0.5 \times \left( \frac{a}{\sqrt{2}} - \frac{\sqrt{2}D}{\sqrt{3}} \right) \left( \frac{a}{2} - \frac{D}{\sqrt{3}} \right)}{\frac{a}{\sqrt{2}} \times \frac{a}{2}} = \left( 1 - \frac{2D}{a\sqrt{3}} \right)^2. \quad (26)$$

## References

- [1] Fleck, N.A., Deshpande, V.S., Ashby, M.F.: Micro-architected materials: past, present and future. *Proceedings of the Royal Society A: Mathematical, Physical and Engineering Sciences* **466**(2121), 2495–2516 (2010)
- [2] Zhu, L., Li, N., Childs, P.: Light-weighting in aerospace component and system design. *Propulsion and Power Research* **7**(2), 103–119 (2018)
- [3] Ge, C., Dong, H., Li, Z., Yu, C., Wang, Z., Sun, Y., Huang, Y., Zhao, T., Li, Y., Wang, L.: Bioinspired 3d printed metamaterial for wideband microwave absorption and aerodynamic efficiency. *Composites Science and Technology* **257**, 110846 (2024)
- [4] Guo, P., Wu, Y., Chen, R., Lu, B., Jia, Y., Zhang, W., Cao, B., Yu, S., Wei, J.: Development of strong, stiff and lightweight compression-resistant mechanical metamaterials by refilling tetrahedral wireframes. *Virtual and Physical Prototyping* **19**(1), 2365852 (2024)
- [5] Cai, Y., Wang, Z., Liu, G., Qian, H., Jiang, Y.: Dual-functional quasi-zero stiffness metamaterial for vibration isolation and impact attenuation. *International Journal of Mechanical Sciences*, 110418 (2025)
- [6] Zhang, W., Xu, J.: Advanced lightweight materials for automobiles: A review. *Materials and Design* **221**, 110994 (2022)
- [7] Tilley, R., Holmes, D., Pickering, E., Woodruff, M.: 3d printed metamaterials for energy absorption in motorsport applications. *International Journal of Automotive Technology* **25**(6), 1529–1540 (2024)

- [8] Satpati, A., Maurizi, M., Yao, D., Kim, S., Wu, H.F., Lee, E.C., Zheng, X.R.: Multi-objective automatic discovery of optimized metamaterials for varying velocity impact protection. *Materials & Design*, 114657 (2025)
- [9] He, Y., Lu, G., Wang, T., Wang, L., Tse, K.M.: Optimized hexagonal perforated honeycomb–chiral metamaterial for multidirectional energy absorption. *International Journal of Mechanical Sciences*, 110521 (2025)
- [10] Al-Ketan, O.: Additive manufacturing-assisted casting of 3d micro-architected heat sinks. *Materials Letters* **379**, 137641 (2025)
- [11] Montemurro, M., Refai, K., Catapano, A.: Thermal design of graded architected cellular materials through a cad-compatible topology optimisation method. *Composite Structures* **280**, 114862 (2022)
- [12] Wang, Y., Sha, W., Xiao, M., Gao, L.: Thermal metamaterials with configurable mechanical properties. *Advanced Science* **11**(40), 2406116 (2024)
- [13] Chen, M., Zhang, J., Shen, X., Zhu, G., Li, B.: Metamaterials based on solid composites enable continuous and tunable thermal conductivity anisotropy for thermal management applications. *Device* **2**(10) (2024)
- [14] Veloso, F., Gomes-Fonseca, J., Morais, P., Correia-Pinto, J., Pinho, A.C., Vilaça, J.L.: Overview of methods and software for the design of functionally graded lattice structures. *Advanced Engineering Materials* **24**(11), 2200483 (2022)
- [15] Qian, M., Huang, S., Xiang, Z., Liu, L., Yu, Y., Zhang, J.: The effect of porous lattice structures on jet impingement heat dissipation performance. *International Journal of Thermal Sciences* **217**, 110071 (2025)
- [16] Wadley, H.N., Queheillalt, D.T.: Thermal applications of cellular lattice structures. In: *Materials Science Forum*, vol. 539, pp. 242–247 (2007). Trans Tech Publications
- [17] Kim, T., Zhao, C., Lu, T., Hodson, H.: Convective heat dissipation with lattice-frame materials. *Mechanics of Materials* **36**(8), 767–780 (2004)
- [18] Ejlali, A., Ejlali, A., Hooman, K., Gurgenci, H.: Application of high porosity metal foams as air-cooled heat exchangers to high heat load removal systems. *International Communications in Heat and Mass Transfer* **36**(7), 674–679 (2009)
- [19] Qian, M., Li, J., Xiang, Z., Dong, Z., Xiao, J., Hu, X.: Study on heat dissipation performance of a lattice porous structures under jet impingement cooling. *Case Studies in Thermal Engineering* **49**, 103244 (2023)
- [20] Shahrzadi, M., Emami, M.D., Akbarzadeh, A.: Heat transfer in bcc lattice materials: Conduction, convection, and radiation. *Composite Structures* **284**, 115159 (2022)
- [21] Vaissier, B., Pernot, J.-P., Chougrani, L., Véron, P.: Parametric design of graded truss lattice structures for enhanced thermal dissipation. *Computer-Aided Design* **115**, 1–12 (2019)
- [22] Piacquadio, S., Schirp-Schoenen, M., Mameli, M., Filippeschi, S., Schröder, K.-U.: Experimental analysis of the thermal energy storage potential of a phase change material embedded in additively manufactured lattice structures. *Applied Thermal Engineering* **216**, 119091 (2022)

- [23] Deshpande, V., Ashby, M., Fleck, N.: Foam topology: bending versus stretching dominated architectures. *Acta Materialia* **49**(6), 1035–1040 (2001)
- [24] Zhang, Q., Li, B., Zhou, S., Luo, M., Han, F., Chai, C., Wang, J., Yang, X.: Superior energy absorption characteristics of additively-manufactured hollow-walled lattices. *International Journal of Mechanical Sciences* **264**, 108834 (2024)
- [25] Wang, Z., Jiang, X., Yang, G., Song, B., Sha, H.: Design and mechanical performance analysis of t-bcc lattice structures. *Journal of Materials Research and Technology* **32**, 1538–1551 (2024)
- [26] Gorgularslan, R.M.: Multi-objective design optimization of additively manufactured lattice structures for improved energy absorption performance. *Proceedings of the Institution of Mechanical Engineers, Part C: Journal of Mechanical Engineering Science* **236**(1), 3–15 (2022)
- [27] Nasrullah, A.I.H., Santosa, S.P., Dirgantara, T.: Design and optimization of crashworthy components based on lattice structure configuration. In: *Structures*, vol. 26, pp. 969–981 (2020). Elsevier
- [28] Murugan, R., Doutre, P.-T., Vignat, F., et al.: Design and analysis of an automotive crash box using strut-based lattice structures. *Journal of Computational and Nonlinear Dynamics* **19**(12) (2024)
- [29] Al-Saedi, D.S., Masood, S., Faizan-Ur-Rab, M., Alomarah, A., Ponnusamy, P.: Mechanical properties and energy absorption capability of functionally graded f2bcc lattice fabricated by slm. *Materials and Design* **144**, 32–44 (2018)
- [30] Kappe, K., Hoschke, K., Riedel, W., Hiermaier, S.: Multi-objective optimization of additive manufactured functionally graded lattice structures under impact. *International Journal of Impact Engineering* **183**, 104789 (2024)
- [31] Rahimi, S., Asghari, M.: Design and evaluation of two proposed hybrid fcc-bcc lattice structures for enhanced mechanical performance. *Heliyon* **11**(1) (2025)
- [32] Alkhatib, S.E., Karrech, A., Sercombe, T.B.: Isotropic energy absorption of topology optimized lattice structure. *Thin-Walled Structures* **182**, 110220 (2023)
- [33] Yin, H., Zheng, X., Wen, G., Zhang, C., Wu, Z.: Design optimization of a novel bio-inspired 3d porous structure for crashworthiness. *Composite Structures* **255**, 112897 (2021)
- [34] Costa, M., Sohoulı, A., Suleman, A.: Multi-scale and multi-material topology optimization of gradient lattice structures using surrogate models. *Composite Structures* **289**, 115402 (2022)
- [35] Xiao, Y., Long, H., Lu, S., Liang, D., Wen, X., Hu, H.: Optimization of crashworthiness of cfrp thin-walled beams filled with aluminium honeycomb based on surrogate model. *International Journal of Crashworthiness* **29**(2), 237–246 (2024)
- [36] Tan, H., He, Z., Li, E., Cheng, A., Chen, T., Tan, X., Li, Q., Xu, B.: Crashworthiness design and multi-objective optimization of a novel auxetic hierarchical honeycomb crash box. *Structural and Multidisciplinary Optimization* **64**(4), 2009–2024 (2021)
- [37] Wang, L.-Q., Tong, J.-Z., Pan, Z.-S., Evans, K.E., Shen, J.: Poisson’s ratio control in auxetic metamaterials under large tensile strains. *International Journal of Mechanical Sciences*, 110637 (2025)

- [38] Yang, M., Han, B., Su, P., Zhang, Q., Zhang, Q., Zhao, Z., Ni, C., Lu, T.J.: Crashworthiness of hierarchical truncated conical shells with corrugated cores. *International Journal of Mechanical Sciences* **193**, 106171 (2021)
- [39] Costas, M., Diaz, J., Romera, L., Hernandez, S.: A multi-objective surrogate-based optimization of the crashworthiness of a hybrid impact absorber. *International Journal of Mechanical Sciences* **88**, 46–54 (2014)
- [40] Xu, P., Yang, C., Peng, Y., Yao, S., Zhang, D., Li, B.: Crash performance and multi-objective optimization of a gradual energy-absorbing structure for subway vehicles. *International Journal of Mechanical Sciences* **107**, 1–12 (2016)
- [41] Pasvanti, N., Psarros, A., Korbetis, G., Vlahinos, A., Mihailidis, A.: Lattice structures modeling: introduction to homogenization. In: *Proceedings of the 8th Before Reality Conference*. Munich, Germany (2019)
- [42] Wu, Y.: Modeling and analysis for unit cell size, material anisotropy and material imperfection effects of cellular structures fabricated by powder bed fusion additive manufacturing. University of Louisville (2020)
- [43] Dassault Systèmes: Abaqus/Explicit
- [44] ANSYS, Inc.: ANSYS Fluent
- [45] Chin, S.Y., Dikshit, V., Meera Priyadarshini, B., Zhang, Y.: Powder-based 3d printing for the fabrication of device with micro and mesoscale features. *Micromachines* **11**(7), 658 (2020)
- [46] Moylan, S., Slotwinski, J., Cooke, A., Jurens, K., Donmez, M.A.: An additive manufacturing test artifact. *Journal of research of the National Institute of Standards and Technology* **119**, 429 (2014)
- [47] Okawa, T., Asano, H., Ito, K., Mori, S., Umekawa, H., Matsumoto, R., Pyeon, C.H., Ito, D.: Fundamentals for power engineering. In: *Fundamentals of Thermal and Nuclear Power Generation*, pp. 77–226. Elsevier, ??? (2021)
- [48] Zephyrhills, I.M.G.: What Speed Do Most Car Accidents Happen At? Accessed: 2025-08-08. <https://www.impactmedicalgroup.com/2023/04/11/what-speed-do-most-car-accidents-happen-at/>
- [49] Pays, J.: Sarasota Attorney Explains How Vehicle Speed Impacts Rear-End Collisions. Accessed: 2025-08-08. <https://www.justicepays.com/news/sarasota-attorney-explains-how-vehicle-speed-impacts-rear-end-collisions/>
- [50] Li, Q., Magkiriadis, I., Harrigan, J.J.: Compressive strain at the onset of densification of cellular solids. *Journal of Cellular Plastics* **42**(5), 371–392 (2006)
- [51] Tan, P.J., Harrigan, J.J., Reid, S.R.: Inertia effects in uniaxial dynamic compression of a closed cell aluminium alloy foam. *Materials Science and Technology* **18**(5), 480–488 (2002)